Arctic Delta Reduced Complexity Model and its Reproduction of Key Geomorphological Structures

Ngai-Ham Chan[1], Moritz Langer[2,3], Bennet Juhls[2], Tabea Rettelbach[2,4], Paul Overduin[2], Kimberly Huppert[1], and Jean Braun[1]

[1]German Research Centre for Geosciences GFZ, Telegrafenberg, 14473 Potsdam, Germany
[2]Alfred Wegener Institute for Polar and Marine Research, Telegrafenberg, 14473 Potsdam, Germany
[3]Geography Department, Humboldt-Universität zu Berlin, Rudower Chaussee 16, 12489 Berlin, Germany
[4]Institute of Geosciences, University of Potsdam, Karl-Liebknecht-Str. 24-25, 14476 Potsdam, Germany

Correspondence: Ngai-Ham "Erik" Chan (echan@gfz-potsdam.de)

Abstract. Arctic river deltas define the interface between the terrestrial Arctic and the Arctic Ocean. They discharge sediments, nutrients, and soil organic carbon to the Arctic Ocean and provide key stratigraphic records of permafrost landscape evolution. As the climate warms, the future evolution of Arctic deltas will likely take a different course, with implications both local in scale and on the wider Arctic Ocean. One important way to understand and predict the evolution of Arctic deltas is through

5   numerical models. Here we present ArcDelRCM.jl, an improved reduced complexity model (RCM) of arctic delta evolution based on the DeltaRCM-Arctic model (Lauzon et al., 2019). We have rewritten the DeltaRCM-Arctic model entirely in the Julia language and the final ArcDelRCM.jl model retains the option to execute as the former. Unlike previous models, ArcDelRCM.jl is able to replicate an important and ubiquitous feature observed in Arctic deltas — the underwater ramps extending from the shoreline of deltas tens of kilometres towards the ocean at a depth of roughly 2 m. This feature may form a buffer between ocean

10   processes and the land portions of the deltas. We have found that the delayed breakup of bed-fast ice on and around the deltas is ultimately responsible for the development of the ramp feature. However, changes made to the modelling of permafrost erosion and protective effects of bed-fast ice are also important contributors. Through a simple graph analysis performed on ensemble runs, including the non-Arctic DeltaRCM (Liang et al., 2015b), we found that the Arctic processes considered in all the models and modifications did not lead to significant differences in the channel structures. Moreover, we found that the summer months

15   contribute significantly to the growth and evolution of Arctic deltas, thus should not be neglected in simulations. Finally, we tested a strong climate-warming scenario on the simulated deltas of ArcDelRCM.jl. We found that the ramp features degrade on the time scale of centuries and effectively disappear in under a millennium. Ocean processes, which are not included in these models, may further shorten the time scale. With the degradations of the ramps, any dissipative effects on wave energy they offered would also decrease. This could expose the sub-aerial parts of the deltas to increased coastal erosion, thus impacting

20   permafrost degradation, nutrients and carbon releases.

1 Introduction

Arctic deltas are key interfaces between permafrost landscapes and the Arctic Ocean. They act as records and filters of the sediments and nutrients that originated from the Arctic and sub-Arctic regions — regions that contain a substantial portion of the Earth's soil organic carbon (Hugelius et al., 2014; Schuur et al., 2015) — which could potentially exacerbate climate

25 warming through positive feedback. As the permafrost thaws and the Arctic ocean trends towards being free of ice, especially under amplified warming in polar regions (Stocker, 2014), Arctic deltas will likely be affected and their evolution may change course. On a local level, the ecosystems surrounding Arctic deltas will also face significant impacts as a result of climate change (Pisaric et al., 2011).

Numerical models are important tools for understanding and predicting the changes that Arctic deltas face. Due to the com-
30 plexity of the system (which involves permafrost, flow on low-slope environments, ice cover, spring floods and more), delta models are typically divided into two classes. The first is built on physically-based equations, simplified to be computationally tractable (e.g., models involving Delft 3D; Lesser et al., 2004). They are able to more directly simulate delta dynamics, but at a cost of computational resources and the ability to cover time scales of years or longer. To address these issues, the second class of models – reduced complexity models (RCMs) – simulate phenomenological processes of arctic delta evolution using rule
35 based trajectories of cellular automata. The rules governing the automata units are typically informed by physical equations under specific sets of conditions and by empirical observations. Due to the simplified construct, there are greater flexibilities in choosing the spatial and temporal step sizes, resulting in much greater spatial and temporal coverage whilst keeping computational requirements feasible. One such RCM is the DeltaRCM (Liang et al., 2015b), the Arctic extension of which (called DeltaRCM-Arctic; Lauzon et al., 2019) will serve as the starting point of our work herein.

40 DeltaRCM and its Arctic extension have been demonstrated to efficiently (in terms of computation) reproduce numerous observed features of natural and experimental deltas (Liang et al., 2015b, a; Lauzon et al., 2019; Piliouras et al., 2021). Our goal is to build upon previous work to reproduce another important feature ubiquitous to Arctic deltas — the 2-m ramps, which we will interchangeably refer to as "ramp features", or simply "ramps". Figure 1 shows an example of such a ramp feature, which dips gradually from below the sea surface to roughly 2-metre depth, but with localised variations on the order
45 of a metre. They are believed to be related to winter ice cover, have an elevation that approximately matches the maximum winter ice thickness, and extend from the above-water shoreline of Arctic deltas over tens of kilometres towards the open ocean (Reimnitz, 2002). They are additionally characterised by grounding of ice in winter, leading to the preservation of permafrost, which can be an important factor in keeping Arctic deltas stable. Therefore, the ramp features, aside from being an integral part of Arctic deltas, may also play an important role in protecting Arctic shorelines from coastal erosion (Dean and Dalrymple,
50 2002) and could enhance carbon sequestration (Overeem et al., 2022). Moreover, the shallow-water platform provided by the ramp could play an important role in the surrounding ecosystems (Lopez et al., 2006). Capturing the ramp features is thus an important building block of modelling Arctic deltas.

To develop ArcDelRCM.jl, we start by rewriting the DeltaRCM base and its Arctic extension in Julia, which has comparable performance as C and FORTRAN but retains the syntactical convenience of MATLAB and Python. We then make a series of

Earth **Surface**
Dynamics
Discussions
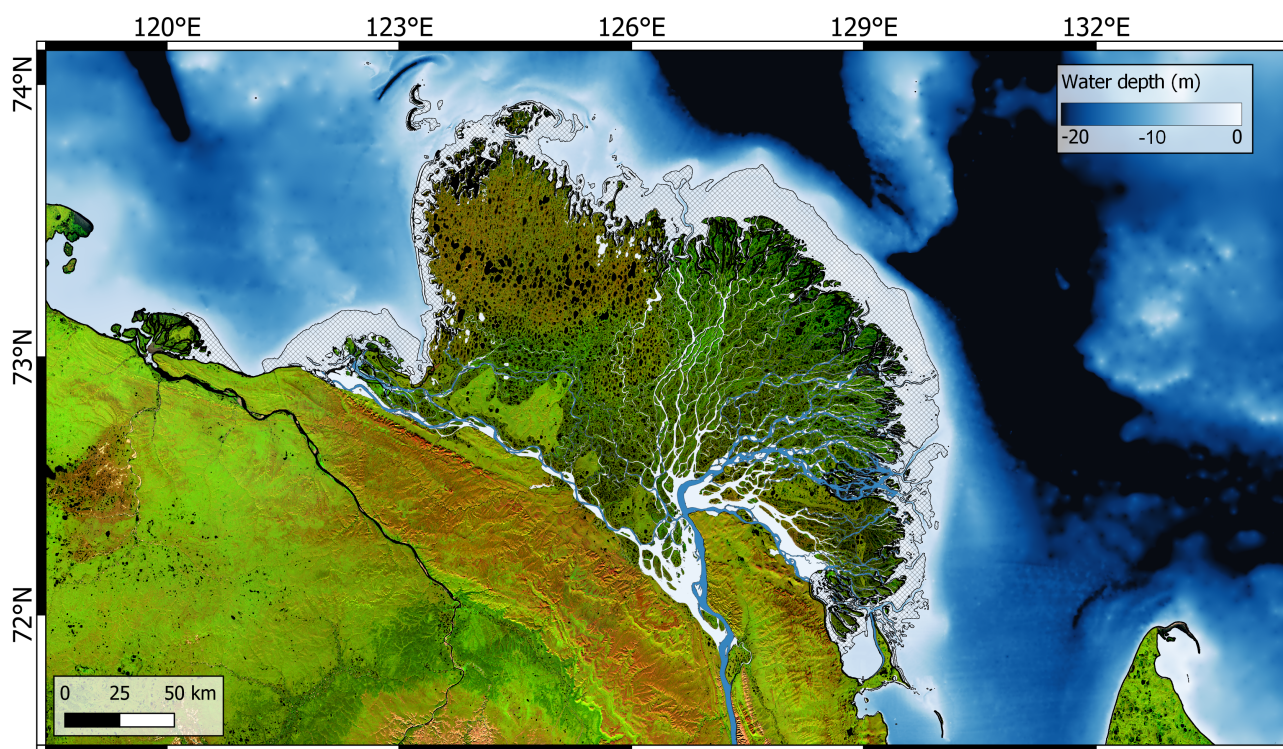
Figure 1. Map of the Lena Delta and the bathymetry of the southern Laptev Sea region (Fuchs et al., 2021). The orange-to-green relief shows the subaerial portion of the Lena Delta and its surrounding land. The blue-to-white colour scale shows the bathymetry. Dark blue channels within the delta show deep channels that do not freeze in winter (Juhls et al., 2021). Light blue within the delta shows the maximum channel area during the spring flood. The hashed area displays the shallow water 2-m ramp feature. Some deeply incised channels are visible within the ramp feature. The land area relief is visualised in a false colour Landsat-8 mosaic, courtesy of the United States Geological Survey, processed in © Google Earth Engine.

55   modifications to the model's rules on physical processes to achieve the ramp features. Moreover, motivated by the high flow rate during summer in large Arctic deltas, we also address the importance of summer months in Arctic delta evolution.

The purpose of this article is two fold. First, we detail the basis and further development of the Arctic-delta model into the ArcDelRCM.jl version written in Julia[1]. Second, we present the model outputs, including ones that are intended to simulate the evolution of large-scale deltas such as the Lena Delta. Through these outputs, we argue for the importance of the summer

60   months in delta evolution and demonstrate the model's capability in reproducing the 2-m ramp. We also attempt to gauge the possible fate of these ramps under a warming climate.

---

[1]The source code is located in a GitLab repository accessible through this link: https://gitlab.com/nhchan/arcdelrcm.jl.

2 Methods

2.1 Description of DeltaRCM(-Arctic)

In this section, we provide an overview of DeltaRCM and its Arctic extension (referred to as "DeltaRCM-Arctic" by Piliouras
65 et al., 2021) based entirely on the original publications (Liang et al., 2015b; Lauzon et al., 2019), the source codes of the
(non-Arctic) DeltaRCM (Liang, 2015; Perignon, 2018), and our observations during the process of reproducing these models
prior to extending them. All modifications we made to the model are left to Section 2.2.

2.1.1 Simulation Domain
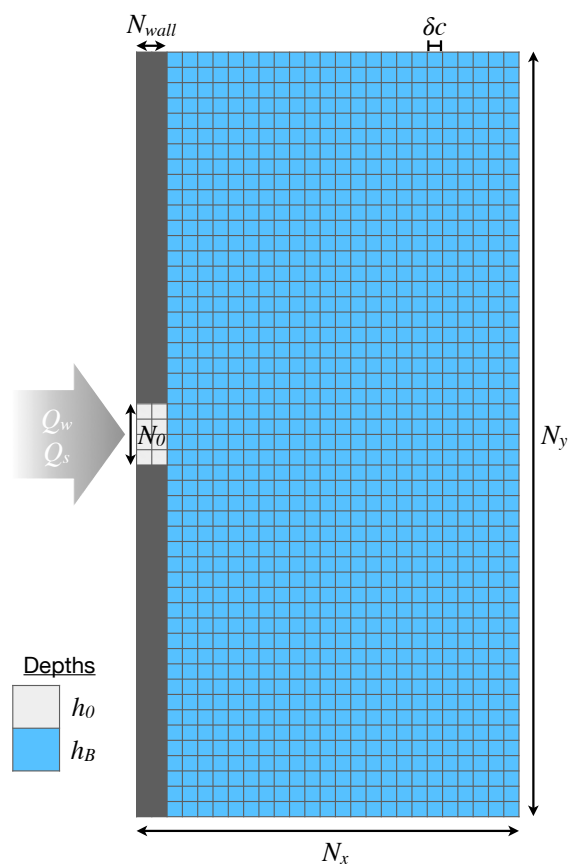
Figure 2. The simulation domain of the delta models. The N values are in terms of the number of grid cells, and the width/length of each
grid cell δc is in metres. The discharges, Q_w and Q_s, enter the domain through the inlet channel on the left N_0 cells wide (light-grey cells).
The depth of an inlet-channel cell is h_0, and the depth of an ocean-basin cell is h_B.

In the most basic setup (Figure 2), the simulation domain consists of a rectangular grid of N_x by N_y cells (typically,
$N_y = 2N_x$). Each cell is a square with a width of δc. Along the y dimension, the first N_{wall} (typically 3) cells in the x direction
are defined as the inlet wall, which are impermeable and static. Centred around the $\left(\frac{1}{2}N_y\right)^{\text{th}}$ cell, there is an opening in the
inlet wall N_0 cells wide, from where the water (volume) discharge, Q_w, and the sediment (volume) discharge, Q_s, enter the
simulation domain. This opening is the inlet channel.

The domain is initialised with a water-surface elevation of H (typically 0 m, taken to be the sea-surface height), a water depth
of h_B ('B' for ocean basin), and a corresponding bed elevation of $\eta = H - h_B$. Within the inlet channel, an initial surface slope,
S_0, is added to mimic the backwater slope. The same S_0 is also imposed along the path of individual water packets (explained
in the Sect. 2.1.2 below) routed through the domain, so that an averaged, approximate backwater slope is formed in each time
step. An inlet flow depth, h_0, is given and reimposed at the start of each time step, such that the inlet flow speed, u_0, can be
determined in conjunction with Q_w and $N_0 \times \delta c$.

2.1.2 Flow Field

To build the flow field within each time step, the input discharge is divided into n_w (which is 2000 in all examples) packets
and sent through the simulation domain using a weighted random-walk scheme. The weights of each of the eight neighbouring
grid cells are determined by a linear combination of two factors: (i) Water-surface gradient (as a proxy to gravity)

$$w_{i,\text{surface}} = \max(0, -\nabla H_i), \tag{1}$$

where ∇H_i is the gradient of water-surface elevation from the current cell towards its ith neighbouring cell. (ii) Flow depth,
expressed as a resistance measure (as a proxy to inertia), scaled by both the projection of the local flow field to the eight
neighbouring cells and by the distances to those neighbouring cells

$$w_{i,\text{inertia}} = \frac{1}{R_i} \frac{\max(0, \mathbf{q_w} \cdot \mathbf{d}_i)}{\Delta_i}, \tag{2}$$

where $R_i^{-1} = (h_i - h_{\text{ice},i})\left(1 - \frac{h_{\text{ice},i}}{h_i}\right)$ is the flow resistance measure of the ith neighbouring cell, taking into account the full
water depth, h_i, and the portion of it that is ice, $h_{\text{ice},i}$ (Lauzon et al., 2019); $\mathbf{q_w}$ is the unit discharge vector at the current cell
(serving as the flow-direction vector); $\mathbf{d}_i$ is the unit vector pointing from the current cell towards the ith neighbouring cell; and
Δ_i is the distance between the centres of the current cell and that of its ith neighbour. Cells with water depth shallower than 0.1
h_0 (up to a maximum of 0.1 m) are classified as "dry" and thus assigned a weight of zero. Discharge is conserved throughout,
with each packet's contribution (q_w) to each visited grid cell recorded in an additive manner. The total random-walk weight is
combined through a "partitioning coefficient", γ:

$$w_i = \gamma w_{i,\text{surface}} + (1 - \gamma)w_{i,\text{inertia}}. \tag{3}$$

Liang et al. (2015b) described the free parameter γ as a control on the lateral spread of water. By increasing the importance of
the water-surface gradient, its cross-channel component is also emphasised. The value of γ is typically small (e.g., 0.05; Liang

et al. 2015b), and is also given by Liang et al. (2015a) as

$$\gamma = \frac{g\delta c S_0}{u_0^2}, \tag{4}$$

where g is the gravitational acceleration. The latter expression may have arisen from taking the ratio between the pressure gradient and inertia terms (without local acceleration) of the shallow water equations. The latter expression is the version for γ implemented in the source codes of DeltaRCM (Liang, 2015; Perignon, 2018) (resulting in a value of 0.098 in their demonstration cases with 50% sand fraction[2]). In our own experiments mimicking the size and conditions of the Lena Delta, with much larger δc, we have found that $\gamma = 0.135$ (± 0.02) works best in producing the planform of deltas similar to the Lena Delta.

We note that, in practice, "Phase 4: update routing direction" of the model operation described in Liang et al. (2015b) is handled directly by the formulation of random-walk weights in Equation 3 during "Phase 1" described in the same article (Liang et al., 2015b).

The slope S_0 is imposed on the surface elevation along each water packet's path, starting from the edge of the delta, which is defined as any grid cell with water depth $h < 0.1h_0$ and flow speed $u > 0.5u_0$, towards the inlet channel[3]. The full water surface is calculated from averaging the surface-height profiles of all n_w paths of individual water packets passing through the domain during the current time step. Any unvisited pixel during a particular time step will inherit the surface elevation from the previous time step. Finally, the water-surface elevation field H undergoes both spatial and temporal smoothing processes described by Equations 11 and 12 in Liang et al. (2015b) to ensure numerical stability.

Given the existing bed-elevation field, η (either from initialisation or from the previous time step), the water depth is determined from $h = H - \eta$. Using the accumulated q_w from all passing water packets and the flow depth h (minus any portion that is h_{ice}), the flow speed u is calculated. Finally, the direction of flow at each grid cell is the average entry and exit directions of all water packets that passed through that cell (Figure 4 of Liang et al., 2015b).

The flow-field determination process is iterated multiple (n_{iter}) times per time step to suppress any instability due to the randomised nature of the scheme (Liang et al., 2015a). Note that there is one more step that is not documented in the original article, but exists in the non-Arctic source codes (Liang, 2015; Perignon, 2018): the flow field q_w also undergoes an "underrelaxation" identical to that undergone by H (Liang et al., 2015b, Equation 12), except that it is with a different coefficient and is applied between each iteration instead of merely across time steps. The underrelaxation coefficient for the q_w field is 0.9 for the first iteration (in each time step) and $2/n_{iter}$ for all subsequent iterations.

2.1.3 Ice Cover

Lauzon et al. (2019) extended DeltaRCM to simulate Arctic deltas. They simulate only the spring-flood period (assumed to be 10 days). At the beginning of each flood, the maximum ice cover is defined with a pair of parameters: maximum ice thickness,

---

[2]Note that their S_0 is influenced by the sand fraction, and can vary by up to a factor of 3 between $0 - 100\%$ sand fractions (Liang, 2015; Perignon, 2018). This contributes strongly, through γ, to how the sand/mud fractions influence the planform of the delta, between fan-like and elongated channels-like.

[3]In the published version of Liang et al. (2015b), the water-depth condition is given as having the bed elevation $\eta_{shore} = H_{sea-level} - 0.9h_0$, or equivalently, $h = 0.9h_0$. That is a typo, and the factor of 0.9 should have been 0.1, based on the source codes of DeltaRCM.

$h_{\text{ice,max}}$, and maximum ice extent, f_{ice}, which is a fraction between 0 and 1. At maximum, ice thickness is $h_{\text{ice,max}}$ everywhere
130 except on "dry" grid cells and except in cells within $(1-f_{\text{ice}})$ of the mean distance between the inlet channel and the (average)
coast of the delta. To improve simulation stability, a taper from 0 to $h_{\text{ice,max}}$ over the equivalent of 10 δc is imposed from the
edge of the ice-free zone towards the ocean. For similar purposes, h_{ice} may not exceed 99% of the local water depth[4].

Two processes contribute additively to the melting of the ice: discharge-based heat flux and atmospheric heat. The former is
given by Searcy et al. (1996) (as cited by Lauzon et al., 2019, supplementary material) as

$$\left(\frac{dh_{\text{ice}}}{dt}\right)_{\text{discharge}} = -\frac{\rho_w}{\rho_i}\frac{c_p C_s u \Delta T}{L_f},\tag{5}$$

where $\rho_w = 1000\ \text{kg m}^{-3}$ and $\rho_i = 917\ \text{kg m}^{-3}$ are the densities of water and ice, respectively, $c_p = 4184\ \text{J kg}^{-1}\ \text{K}^{-1}$ is the
specific heat capacity of water, $C_s = 2 \times 10^{-4}$ is the heat transfer coefficient (Searcy et al., 1996), ΔT is the temperature
difference between the melting point of water and the discharge water (assumed to be 4°C in DeltaRCM-Arctic), and $L_f =$
$3.3355 \times 10^5\ \text{J kg}^{-1}$ is the latent heat of fusion of water. Discharge-based melt is calculated using the above expression with
140 the flow speed field u at the current time step.

The atmospheric contribution to the ice melt is given by

$$\left(\frac{dh_{\text{ice}}}{dt}\right)_{\text{atmospheric}} = -a\frac{h_{\text{ice,max}}}{t_{\text{melt}}},\tag{6}$$

where t_{melt} is the period during which the entire ice thickness would melt due to atmospheric heat alone, and a is a scaling
factor, between 0 and 1, to tune the contribution of atmospherically induced melting towards the total melt. In the model result
145 of Searcy et al. (1996), $a \approx 0.58$, and in Piliouras et al. (2021), $a = 0.5$. In DeltaRCM-Arctic, t_{melt} is taken to be 10 days (i.e.,
the entire simulation period for each model year) (Lauzon et al., 2019; Piliouras et al., 2021).

2.1.4 Sediments and Permafrost

The sediment entering the delta in DeltaRCM(-Arctic) is split into two categories: sand (representing bed load) and mud
(representing suspended load). Their relative fraction of the total is given by the "sand-fraction" parameter, f_{sand}. Like the
150 water discharge, the (volume) discharge of *each* sediment category is divided into n_s packets ($n_s = 2000$ in all simulations).
In each time step, after the flow field has been determined, these packets are routed through the simulation domain using the
same weighted random walk scheme described in Equation 2 (but not Equation 1). The only exception is for bed-load ("sand")
packets, for which the flow-resistance measure, R_i^{-1} acquires an exponent of 2 (Liang et al., 2015b).

Deposition and erosion of sediments are determined by a set of threshold relations detailed in Liang et al. (2015b, Sect. 3.2.5).
155 As each sediment packet passes through a grid cell, local conditions are checked against the thresholds and an appropriate
volume of sediments is taken up by or deposited from the packet. The bed elevation η and flow speed u (and thus the "dry"
flag, if applicable) are updated after each erosion/deposition event. This way, the next visiting packet will not over-erode/-
deposit. A hard limit is imposed so that no single sediment packet can change the bed elevation by more than 25% of the total
water depth h.

---

[4]We used 99.99% in ArcDelRCM.jl.

160   Deposited sediments are tracked and stored in a grid with the same lateral spatial coverage as the simulation domain (N_x by N_y), and with a depth-wise dimension of δz per cell. After all sediment packets have passed through during one time step, any bed-elevation gains are added to the sediment grid. Each of these added grid elements records the "sand fraction" (i.e., the relative fraction of sand in the total volume of sand and mud) of all sediments deposited by all passing packets. Figure D1 shows our code's implementation of this, which includes storage of additional quantities. Grid cells corresponding to eroded

165   sediments (i.e., the volume picked up by passing water packets) are simply removed.

In DeltaRCM-Arctic, Lauzon et al. (2019) assume a constant active layer (or thaw depth) of 0.5 m. A sediment cell is considered a permafrost cell if it has remained below the thaw depth for at least two years. If a column of sediment contains 75% permafrost cells or if the permafrost cells amount to $\geq 75\%$ of the inlet-channel depth h_0, the corresponding planar grid cell (i.e., in the x, y dimensions) are flagged as a "permafrost cell".

170   To simulate the erosion of a permafrost bed, DeltaRCM-Arctic (Lauzon et al., 2019) used a multiplicative erodibility factor, $E \leq 1$, to scale the erosional thresholds (given in Liang et al., 2015b, Sect. 3.2.5) of permafrost grid cells, such that erosion is harder to achieve.

2.1.5 Bed Diffusion and Shore/Bank Migration

Immediately after each round of sediment packet routing, a bed-diffusion process is applied "to take into account the influence

175   of topographical slope on sediment flux" (Liang et al., 2015b). This is achieved by calculating the "diffusive sand flux"

$$q_{\text{sand,diff}} = \alpha |\nabla \eta| q_{\text{sand}} , \tag{7}$$

where α is a coefficient set to 0.1 in all demonstrated cases, $|\nabla \eta|$ is the absolute slope of the bed, and q_{sand} is the sand flux into and out of the grid cell in concern. Both $|\nabla \eta|$ and q_{sand} are calculated across the boundary between the grid cell in concern and each of its neighbouring cells. Contributions of each of the neighbours are summed to give $q_{\text{sand,diff}}$, which is then used to

180   determine the diffusion-induced bed-elevation change $\Delta \eta$ of the grid cell in concern. In DeltaRCM-Arctic, α is further scaled by the erodibility factor, E.

After each full update of the water surface and each full update of the bed elevation, shoreline or river-bank migration is performed. In the source codes of DeltaRCM, this is referred to as "flood correction" (Liang, 2015; Perignon, 2018), but not explicitly described in the article (Liang et al., 2015b). This means that any "dry" grid cells are refilled with water when one

185   or more neighbouring cells have higher water surfaces. We assume that DeltaRCM-Arctic also inherited this mechanism, but excluded the ice thickness h_{ice} from the water-surface height (see Sect. 2.2.4 for our interpretation of this).

2.2 Modifications and Interpretations in ArcDelRCM.jl

We completely re-wrote the model in the Julia language, refactoring the algorithm as we saw fit. Partly due to the ("just-in-time" compiled) nature of Julia, ArcDelRCM.jl is able to complete identical simulations in under 50% of the time compared to

190   the MATLAB version of DeltaRCM (Liang, 2015) and under 17% of the time compared to the Python 2 version of DeltaRCM

(Perignon, 2018)[5]. Since we do not have access to the source code of DeltaRCM-Arctic, we have no performance comparisons between the Arctic simulations. Aside from the re-write, we also made significant changes to the model itself to improve its ability to account for processes that are climate-sensitive. We describe them in turn in this section. Three more user-feature additions are described in Appendix A.

2.2.1 Bed-fast Ice Protection and Shielding

Due to the weighted random walk scheme and the limit of h_{ice} to 99.99% of the water depth (for numerical stability), water packets can still go through grid cells where the entire water depth is effectively in the form of ice (albeit with a very small probability, since the un-frozen water depth plays an important role in determining random-walk weights). This can generate unrealistic flow pathways with anomalously high speeds (due to ice constriction) and consequent ice melting. To eliminate this unrealistic behavior, we prohibit flow-speed induced melting when ice is effectively in contact with the bed (i.e., $h_{\mathrm{ice}} \approx h$). We call this "bed-fast ice protection". In the same locations, the cell is considered entirely blocked by bed-fast ice and no erosion or deposition can occur. We call this "bed-fast ice shielding" of the bed.

2.2.2 Time-dependent Thaw Depth

Since we introduced ice protection and ice shielding, we deemed it logically necessary to also introduce a time-dependent thaw depth. We do so according to the Stefan Model (Riseborough et al., 2008; Lunardini, 1981): $X = \sqrt{\frac{2\lambda I}{L}}$, where X is the thaw depth, $\lambda \equiv 2.22\ \mathrm{W\ m^{-1}\ K^{-1}}$ is the thermal conductivity of ice near $0°\mathrm{C}$, $L \equiv 3.3355 \times 10^8\ \mathrm{J\ m^{-3}}$ is the volumetric latent heat of fusion of water, and I is the "positive degree day index", which is the accumulated number of days with positive temperature since winter. Where there is bed-fast ice at the start of the simulation, the thaw depth starts at 0 and I only begins to increment when the ice in the pixel is no longer bed-fast. Otherwise, I starts at 10 days in our standard simulation (see Appendix B for the reason behind this choice). As a result of the time-variable thaw depth, we also redefine a "permafrost" cell in our sediment columns as vertical cells that stayed below the maximum thaw depth (instead of a static active-layer depth of 0.5 m) for at least 2 years.

2.2.3 Permafrost Erosion

To simulate the erosion of the permafrost bed, the original model used a scaled erodibility factor, $E \leq 1$, for grid cells with over 75% permafrost content in the sediment column. With the introduction of time-dependent thaw depth, we find it more self-consistent to check the calculated erosional depth of the grid cell against its corresponding sediment column: If the calculated erosion reaches deeper than the available thawed layers, the erosional depth is limited to the thawed layers only. Whilst the sediment column is immediately updated as a sediment packet passes through, which prevents duplicate erosion/deposition by successive packets, the value of the bed elevation is kept in memory unchanged during each time step, thus tracking the exact

---

[5]Tested on a MacBook Pro laptop with 2.6 GHz 6-Core Intel Core i7 and 32GB of RAM in early 2020.

220 layer that is at the bottom of the thawed section. We thus forgo the use of the erodibility factor, E, although we retained it in the source code for users who opt to run the model as DeltaRCM-Arctic.

2.2.4 Shore/Bank Migration

A "flood correction" mechanism is built into the original, non-Arctic source codes of Delta RCM (Liang, 2015; Perignon, 2018), but not explicitly described in the article of Liang et al. (2015b). This mechanism, which we refer to as "shore/bank

225 migration", ensures that "dry" grid cells are refilled with water when one or more neighbouring cells have higher water surfaces. Without access to the source code of DeltaRCM-Arctic (Lauzon et al., 2019), how they handled the presence of ice in this context is unclear. In ArcDelRCM.jl, we interpret the water surface elevation in this context as the below-ice surface. Therefore, only dry cells with at least one neighbouring cell that has a higher *liquid* water-surface elevation are rewetted.

2.2.5 Time-step Size

230 To keep the simulation numerically stable, the original model determines the time-step size based on the volume of sediments entering the simulation domain. Specifically, $\Delta t = \frac{N_0^2 h_0 \delta_c^2}{10 Q_{s_0}}$ (Liang et al., 2015b). We discovered in our simulations intended to mimic the Lena Delta, where the grid-cell dimensions are several times larger than in Liang et al. (2015b) and Lauzon et al. (2019), that the 10 in the denominator of expression for Δt needed to be increased by a factor of a few. In order to facilitate the use of time-dependent input discharges (described in the next subsection), we let Δt be user-determined, but implemented an

235 internal checking procedure to warn users of potential numerical instability. For this check, we introduce a quantity that we call "scale-height measure": $\zeta \equiv \frac{Q_{s_0} \Delta t}{\delta_c^2 h_B}$. ζ is a rough scaling between the volume of sediment entering through the inlet channel in each time step and the "available" volume of an average single ocean-basin grid cell. Based on experiments with both the dimensions of Liang et al. (2015b), Lauzon et al. (2019), and our Lena-like dimensions, we found that ζ should be $\lesssim 3$ for the model to be numerically stable.

240 ### 2.2.6 Input Discharges as Time Series

In large drainage basins such as the Lena watershed, discharge beyond the spring flooding season remains significant through the summer. In order to capture these deltas' summer evolution, we modify the model to take in time series of input discharges (both water and sediments) and extend the simulation model year to include the summer months. Under this setup, the inlet flow speed, u_0, the inlet flow depth, h_0, and the reference water-surface slope (used as an approximation of the backwater

245 slope), S_0, all become time series themselves and are dependent on the water discharge Q_{w_0} time series[6]. To simplify the process for the user and reduce chances of mistakes, ArcDelRCM.jl users input the minima of u_0, h_0, and S_0, corresponding to the minimum Q_{w_0}. The simulation then uses the time series of Q_{w_0} to calculate the corresponding time series of u_0 and h_0 based on a scaling derived from the Gauckler-Manning formula (Gauckler, 1867; Manning et al., 1890), and of S_0 based on simple geometric arguments. We describe these in order.

---

[6]Static values of these quantities remain possible as inputs in ArcDelRCM.jl.

250 We first assume open-channel flow and that the (overall) channel bed slope is approximately constant. The average flow velocity is given by the Gauckler-Manning formula (Gauckler, 1867; Manning et al., 1890), which, for our purpose and under our assumptions, can be expressed as a proportionality:

$$\bar{u} \propto R_h^{\frac{2}{3}}, \tag{8}$$

where R_h is the hydraulic radius:

255 $$R_h = \frac{A}{P},$$

where A is the cross-sectional area of the channel, and P is the "wetted perimeter" of the channel. Assuming a simplistic, rectangular channel shape, with width, w, and flow depth, h, we have $A = hw$ and $P = 2h + w$. Then, using the expression for discharge, $Q = A\bar{u}$, we calculate the flow depth under some new discharge, Q_n, in relation to an "original" discharge, Q_o, as follows:

260 $$\frac{Q_n}{Q_o} = \frac{A_n \bar{u}_n}{A_o \bar{u}_o} = \frac{h_n \bar{u}_n}{h_o \bar{u}_o} = \frac{h_n \left(\frac{h_n w}{2h_n + w} \right)^{\frac{2}{3}}}{h_o \left(\frac{h_o w}{2h_o + w} \right)^{\frac{2}{3}}} \approx \left(\frac{h_n}{h_o} \right)^{\frac{5}{3}},$$

where we have assumed a constant w and that w is much greater than both h_o and h_n. Similarly, the transformation of $\bar{u}$ from Q_o to Q_n can be calculated, via Equation 8, by

$$\frac{\bar{u}_n}{\bar{u}_o} = \left(\frac{h_n}{h_o} \right)^{\frac{2}{3}}.$$

Given an "original" slope, S_o, corresponding to h_o under the discharge Q_o (with $\bar{u}_o$), one can define a "baseline reach",

265 $L_B \equiv h_o/S_o$, such that the new slope under the discharge Q_n (with h_n and $\bar{u}_n$) can be approximated by

$$S_n \approx \frac{h_n}{L_B}.$$

In the manner described above, the inlet flow depth, the inlet flow speed, and the reference slope corresponding to the input discharge time series, Q_w, can be calculated as long as h_0, u_0, and S_0 corresponding to the minimum Q_w are supplied.

2.2.7 Controls on the Melting of Ice

270 We have added the capability for the users to shift the timing and duration of the ice cover's melt. This modification was motivated by the observations that bed-fast ice just offshore from the delta remains intact longer than the ice cover on the delta, and does not disintegrate until the delta itself is almost ice free. Moreover, based on examainations of satellite imagery, the duration of ice-cover melting on the Lena Delta is closer to 20 days instead of 10 days. An example of such observations is shown in Figure 3. In ArcDelRCM.jl, users can specify the length of the ice-cover melting period, during which atmospheric

275 heat contributes to the melting. Note that flow-speed induced melting is always active, subject to the protection described in Sect. 2.2.1. Users can also shift the onset of the atmospheric melting period so that it is delayed from the start of a model year. Finally, the time-profile of the ice melt can also be specified (e.g., hyperbolic tangent instead of the default linear).
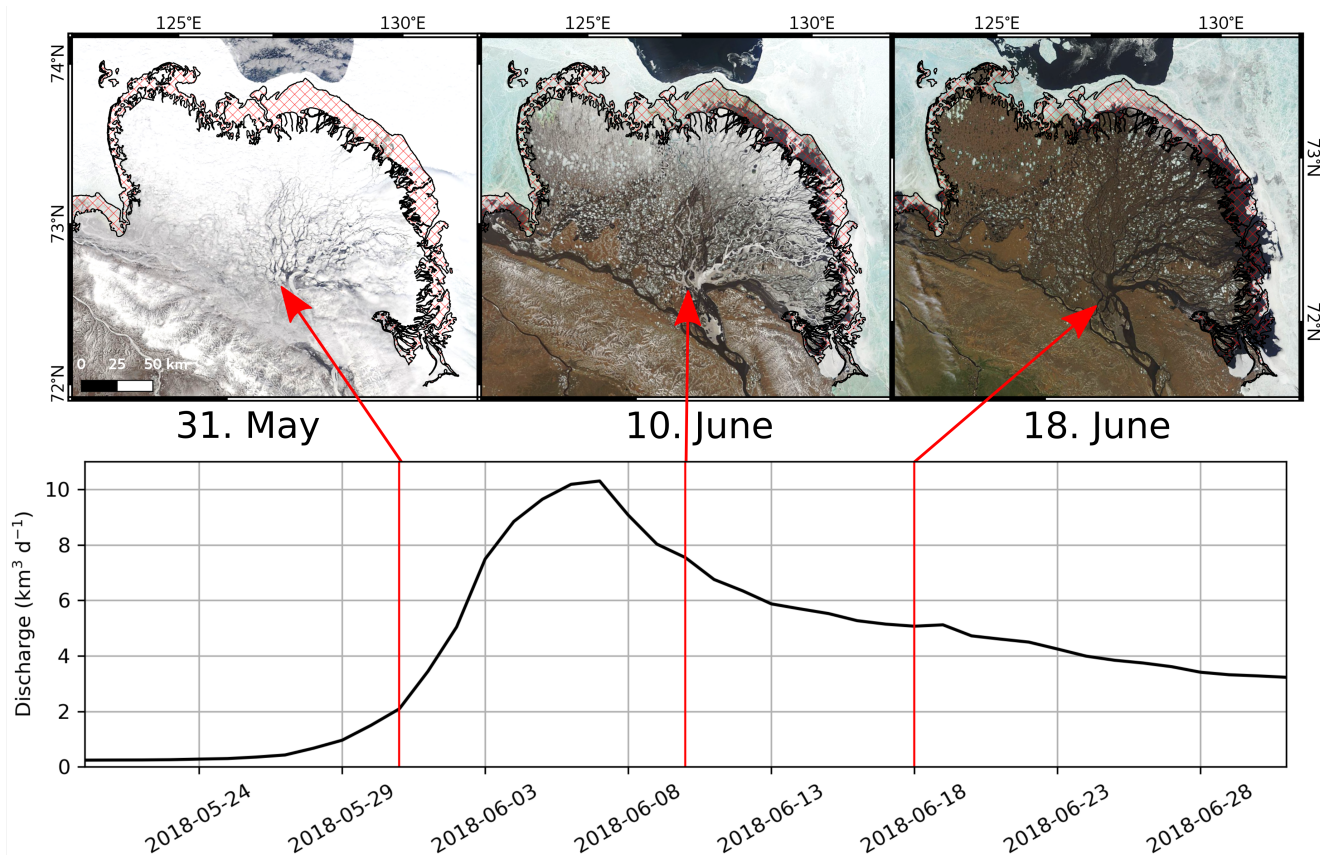
Figure 3. Satellite imagery of the Lena Delta from 2018 showing the delayed break-up of bed-fast ice on the ramp feature. The upper panels show the imagery of the Lena Delta. The hash pattern in red marks the location of the ramp, and the left, middle, and right panels correspond respectively to the start, middle, and completion of ice break-up on the delta itself. The corresponding dates and discharge (measured at Kyusyur station and corrected for the distance to the Lena Delta; Juhls et al., 2020) is shown in the bottom panel, marked by the red arrows. Satellite imagery is acquired by the Moderate Resolution Imaging Spectroradiometer (MODIS) and obtained from NASA Worldview.

3   Results

We present here the outputs of ArcDelRCM.jl and DeltaRCM-Arctic (for comparison), all of which have the following
parameters: $(N_x, N_y) = (150, 300)$, $N_{wall} = 3$, the number of water and sediment packets (sand and mud separately) are
$n_w = n_s = 2000$, and coefficient for bed diffusion $\alpha = 0.1$. Further parameters applicable to individual cases are specified in
the respective subsections below. Any remaining parameter not explicitly listed takes on values given in Liang et al. (2015b).
Note that the colour-blindness friendly colour scheme, uniform across all the filled-contour figures in this section, is chosen to
highlight the per-metre gradation of elevations below the water surface.

3.1   Analogous Setup to DeltaRCM-Arctic Demonstrations

In this subsection, we present comparisons of simulations, run with identical parameters and identical random seeds, in
DeltaRCM-Arctic and ArcDelRCM.jl. Specifically, we adopt $\delta c = 50$ m, $N_0 = 5$, $h_0 = 5$ m, $h_B = 5$ m, $u_0 = 1 \text{ ms}^{-1}$, $S_0 = 1.5 \times 10^{-4}$, $Q_w = 1250 \text{ m}^3\text{s}^{-1}$, $Q_s/Q_w = 0.001$, a sand fraction (of the total sediment volume) of 25%, a maximum ice ex-
tent of 40%, $h_{\text{ice,max}} = 2$ m, a scaling factor for atmospherically induced melting of $a = 0.5$, and $\gamma = 0.0735$. In the case of
DeltaRCM-Arctic, we use an erodibility factor $E = 0.65$, which mimics the restricted erosion of our approach in ArcDelRCM.jl
(Sect. 2.2.3). For ArcDelRCM.jl, we specify $\Delta t = 25000$ s, matching the Δt automatically determined in DeltaRCM-Arctic.
All cases are run for 5000 time steps, with an additional 300 "lead-up" steps under non-Arctic conditions to build up a seed
flow field (following Lauzon et al., 2019; Piliouras et al., 2021).[7]

   The first row of Figure 4 shows the output from DeltaRCM-Arctic (Figure 4a) and ArcDelRCM.jl (Figure 4b). The second
row of Figure 4 shows the output from the same simulations as the first row, but with $h_{\text{ice,max}} = 3$ m (Figures 4c and 4d). The
last row of Figure 4 shows the output of ArcDelRCM.jl under identical configurations as in Figure 4b, except h_B is increased
to 7m in Figure 4e, and the ice extent is increased to 100% in Figure 4f.

   The ramp features form continuous bands around all the deltas in ArcDelRCM.jl except in the case where $h_B = 7$ m, in
which the ramp has nearly vanished (Figure 4e). The ramp appears to be slightly more prominent in the case with 100% ice
extent (Figure 4f) and the case with $h_{\text{ice,max}} = 3$ m (Figure 4d). The deltas of DeltaRCM-Arctic do not show such ramps
(Figure 4a), but rather display lopes or tentacles of "off-shore depositions" (as they are called in Piliouras et al., 2021) around
channel outlets (Figure 4c). As we will explore in the next subsection, we find that the ramp feature results after switching on
the protection of bed-fast ice (Sect. 2.2.1).

3.2   Individual Modifications in ArcDelRCM.jl

Figure 5 shows the effects on the simulated deltas arising from the individual modifications described in Sect. 2.2.1 to 2.2.4.
The model settings are identical to the $h_{\text{ice,max}} = 2$ m cases of Figure 4, but with a different random seed. The random seed
across all cases in Figure 5 are identical, however. All the cases with erosion limited to thawed layers instead of using the
erodibility factor (Sect. 2.2.3) display a greater number of deep channels or channels that are inactive but preserved (Figures 5c

---

[7]We do not find that the lead-up phase has noticeable impacts on the numerical stability or the resulting deltas in our numerical experiments.
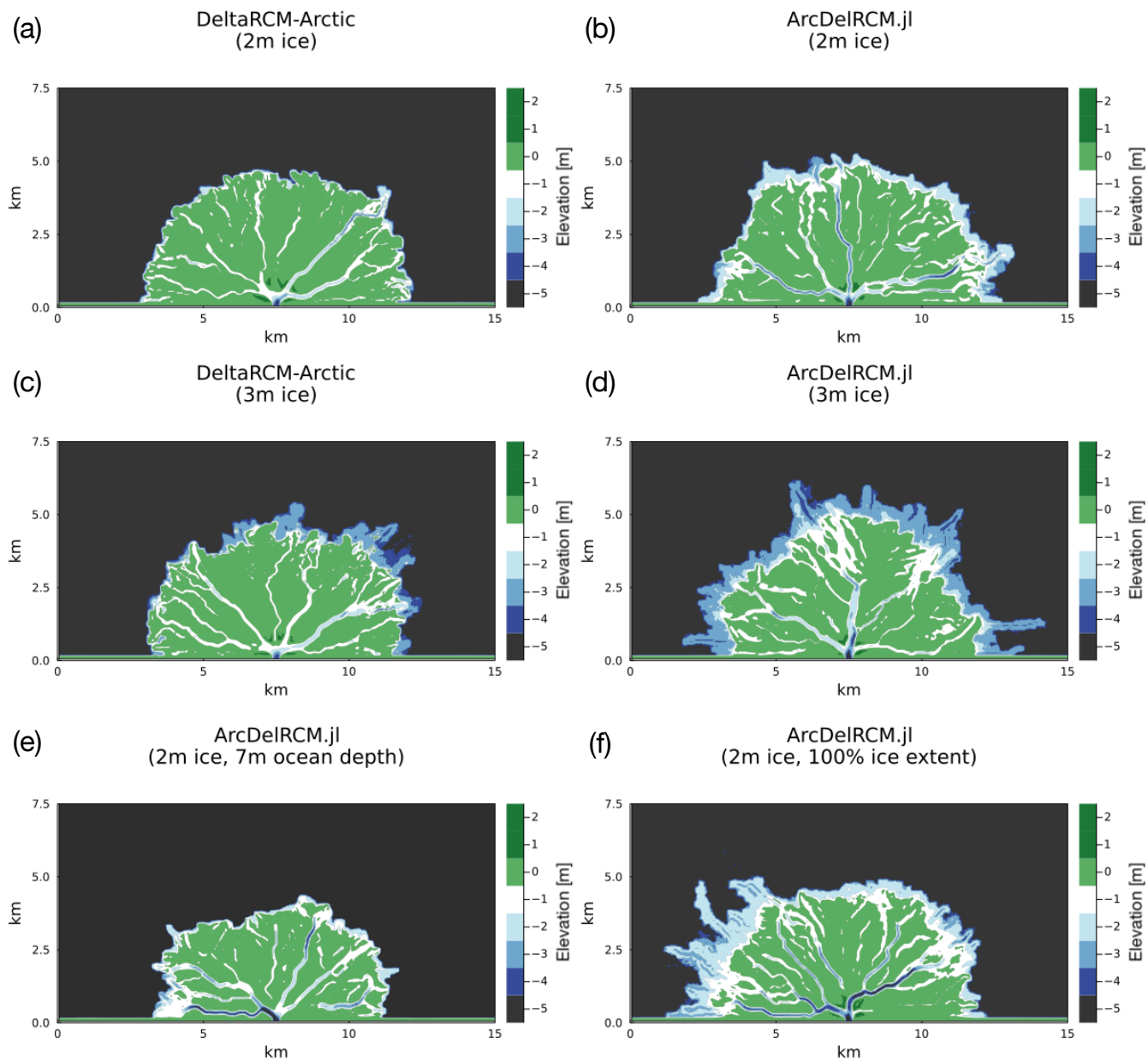
Figure 4. Bed-elevation output of (a, c) DeltaRCM-Arctic and (b, d-f) ArcDelRCM.jl after 5000 time steps (following a 300-step lead up under non-Arctic conditions). All runs have identical parameters (see text for full configuration), except the following differences: (a-b) $h_{\mathrm{ice,max}}$ is 2 m; (c-d) $h_{\mathrm{ice,max}}$ is 3 m; (e) h_B is 7 m; and (f) the ice extent is 100%. Note the depths of the ramp features in panels b and d, which correspond to $h_{\mathrm{ice,max}}$. Tentacle-like "off-shore depositions" (as described in Piliouras et al., 2021) are visible in the $h_{\mathrm{ice,max}} = 3\,\mathrm{m}$ cases of DeltaRCM-Arctic (in panel c) as well as outside the ramp of ArcDelRCM.jl (in panel d). Also, the ramp feature has vanished in panel e, but has become more prominent in panel f.

to 5f). The cases in which the thaw depth is time-dependent (Sect. 2.2.2) appear similar to those with static thaw depths, except

310   with less tentacle-like depositions reaching seaward from channel outlets (Figures 5e and 5f). The case with only ice shielding

of the bed (Sect. 2.2.1) appears to display fewer deep preserved channels and some tentacle-like depositions (Figure 5g), similar

to those in Figures 5e and 5f. The case in which bed-fast ice is protected from flow-induced melt (i.e., ice protection; Sect.

2.2.1) in addition to ice shielding of the bed exhibits a visible 2-m ramp around the delta in addition to small tentacle-like

depositions seaward (Figure 5h). The cases for DeltaRCM-Arctic and the full ArcDelRCM.jl are given for visual comparison

315   (Figures 5a and 5b).

Using the graph algorithms and techniques of Rettelbach et al. (2021), we also calculated a few basic graph metrics for

the individual cases represented in Figure 5, in addition to the non-Arctic DeltaRCM (not shown), each using an ensemble

of 105 realisations to quantify any significant differences in the deltas' topologies. The variability within each of the cases

are far greater than any potential differences between the cases (Figure C1). In other words, all basic metrics are statistically

320   indistinguishable between all cases, including the non-Arctic DeltaRCM one.

3.3 Lena Delta Approximants

We ran simulations that approximate the scale of the Lena Delta, adopting spatial scales that had never been applied to

this model (and its parent models) before. Specifically, we adopt $\delta c = 400$ m, $N_0 = 6$, $h_{0,\min} = 10$ m, $h_B = 15$ m, $u_{0,\min} = 1$ m s^{-1}, $S_{0,\min} = 5 \times 10^{-5}$, $Q_s/Q_w = 3 \times 10^{-4}$ (roughly 10 times the average volume fraction measured in the Lena Delta;

325   Boike et al., 2019), a sand fraction of 20%, a maximum ice extent of 100%, $h_{\mathrm{ice,max}} = 2$ m, the scaling factor for atmospheri-

cally induced melting as $a = 0.5$, $\gamma = 0.135$, and a time step of 1 day.

We ran one batch of simulations for 150 model years. Within this batch, the discharge Q_w is treated differently in order

to highlight the difference it makes in terms of the number of days per simulation year, given realistic $Q_w(t)$. The "full"

simulation cases cover in each model year the 4 months from 1$^{\text{st}}$ June to 30$^{\text{th}}$ September (122 days). In these cases, $Q_w(t)$ is a

330   time series constructed from daily discharge data from the STOLB station near the main channel into the Lena delta (GRDC

Station Data 2903430, 2018), with daily values averaged from 1951 to 1980 inclusive (Figure 6).

The "10-day" cases have two variants: the "constant averaged peak discharge" case (Figure 7a) uses the averaged value from

the peak 10 days of $Q_w(t)$ as the constant discharge; and the "time-variable discharge during peak" case (Figure 7b) uses the

peak 10 days of the $Q_w(t)$ time series as the input discharge. The 10-day peak period is highlighted by a grey band in Figure 6.

335   The full 4-month cases are also divided into two variants: one in which the ice-melt period is 10 days (Figure 7c), similar

to the aforementioned 10-day cases; and one in which the ice-melt period is 20 days long and is delayed by 20 days from the

start of each model year (Figure 7d). In all cases, flow-induced melting is active (where allowed) throughout the whole of the

simulation. We use "ice-melt period" to refer to only the time during which the atmospheric contribution is active (i.e., t_{melt} in

Equation 6).

340   The resulting deltas in the 10-day cases are entirely under water and similar to each other in extent (Figures 7a and 7b). The

4-month cases also produced deltas that are similar in extent with each other (Figures 7c and 7d), but reaching twice as far

from the inlet wall as the 10-day cases. A ramp is also visible around the delta in the case with 20-day ice-melt period delayed
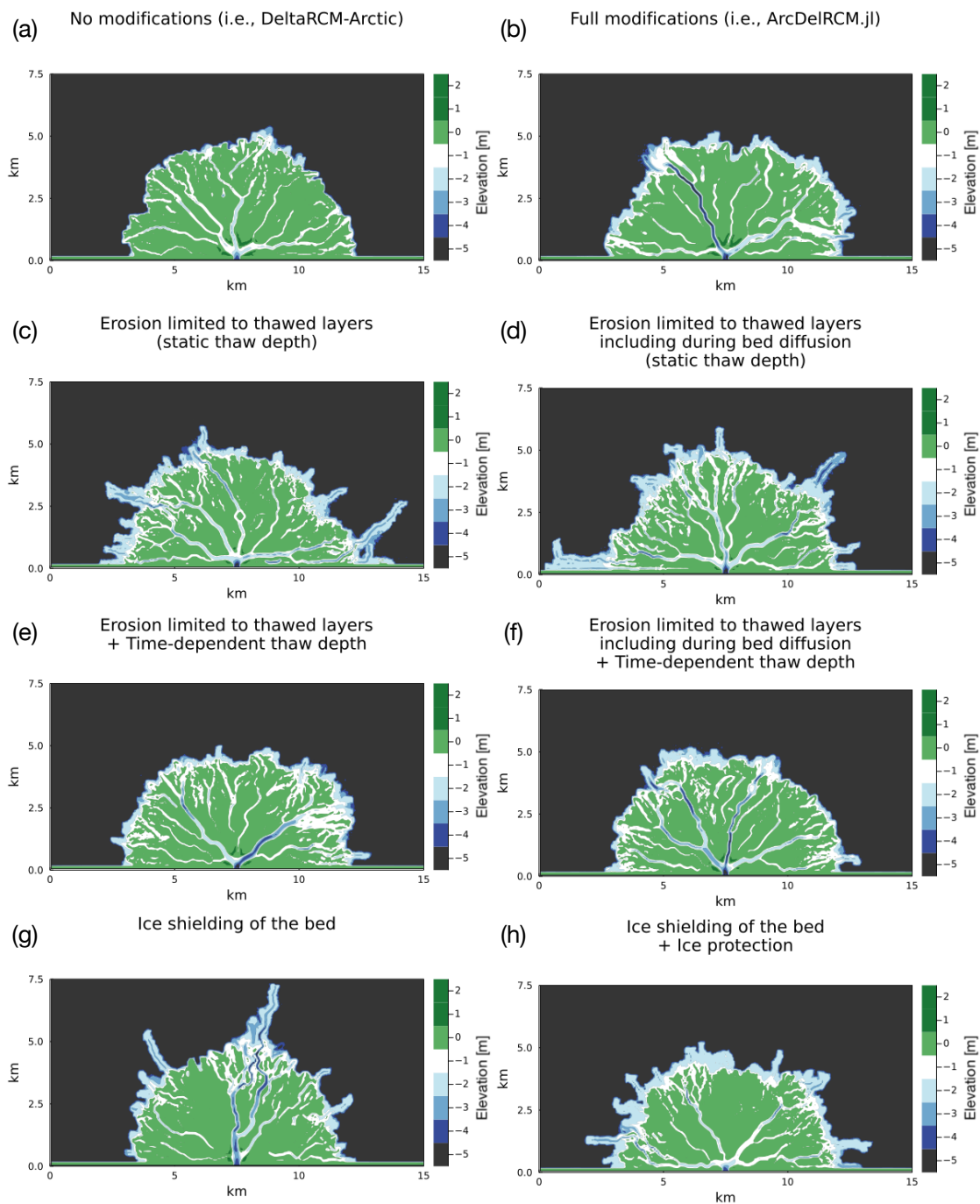
Figure 5. Bed-elevation output of DeltaRCM-Arctic (a), ArcDelRCM.jl (b), and with modifications described in Sect. 2.2.1 to 2.2.4 applied individually or in tandem, as indicated by the title of each panel (c-h). Note the 2 m ramp in the full model and the case in which ice shielding and ice protections are applied together.
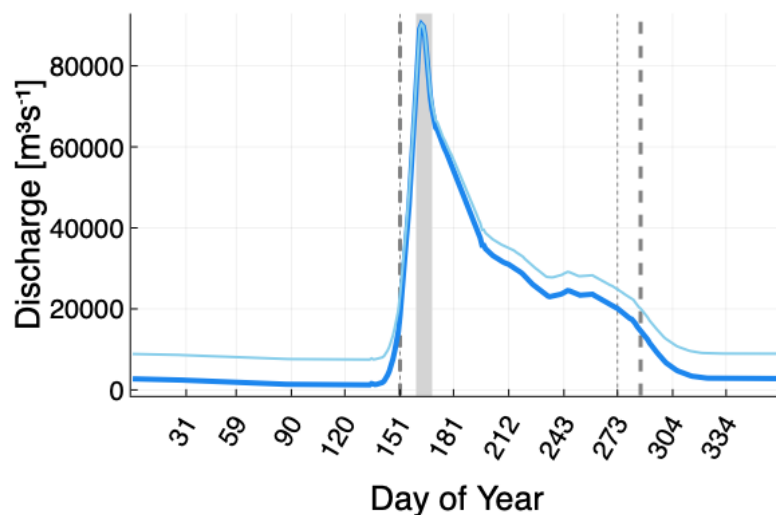
Figure 6. Daily discharge measured at STOLB station (thick blue line; GRDC Station Data 2903430, 2018), averaged from 1951 to 1980 inclusive. Discharge remains over $20000\,\mathrm{m}^3\,\mathrm{s}^{-1}$ during the months from June to September (between the thin grey dotted lines), which is the simulation period for the 4-month Lena-approximant cases. The grey band spans the peak 10 days of discharge. The light-blue, thinner line shows the same discharge pattern, except the overall discharge has been scaled up by 35% (representing the RCP 7 - 8.5 scenario) whilst keeping the peak value and the shape of the curve the same. The period during which discharge is over $20000\,\mathrm{m}^3\,\mathrm{s}^{-1}$ is longer, at 136 days (between the thick grey dash lines).

by 20 days (Figure 7d), albeit being more disrupted by sections with shallower depths ($\sim 1\,\mathrm{m}$; second contour level from the top) than in the small-scale cases in Sect. 3.1.

345 As an additional demonstration of the model in approximating the scale of the Lena Delta, we run the simulation with the same parameters but with $Q_s/Q_w = 3 \times 10^{-5}$, reflecting the measured average volume fraction of sediment to water (Boike et al., 2019). This low sediment-to-water volume fraction requires a much longer run time to produce a delta. Therefore, we ran the simulation for 1200 model years (with the same $\Delta t = 1\,\mathrm{day}$). To further mimic the underlying ocean bathymetry on the Laptev Sea coast, where the Lena Delta is situated, we introduced a gradual tilt of the ocean basin elevation h_B: from 10m

350 at the inlet wall to 20m on the opposite side of the simulation domain. The extent of the tilt and the 20-m maximum h_B is motivated by inspecting the bathymetry of the Laptev Sea coast (Fuchs et al., 2021). The resulting delta is shown in Figure 8. The extent of the delta is similar to the 4-month cases (at 150 model years) in Figure 7, whilst the ramp feature is more prominent than in the other Lena-approximant cases.

3.4 Ramp Feature under a Warming Climate

355 To explore how a warming climate might affect the ramp feature, we continued the simulation of the delta shown in Figure 8 for another 1200 model years. However, for this portion, we adopt an end-member scenario of Representative Concentration
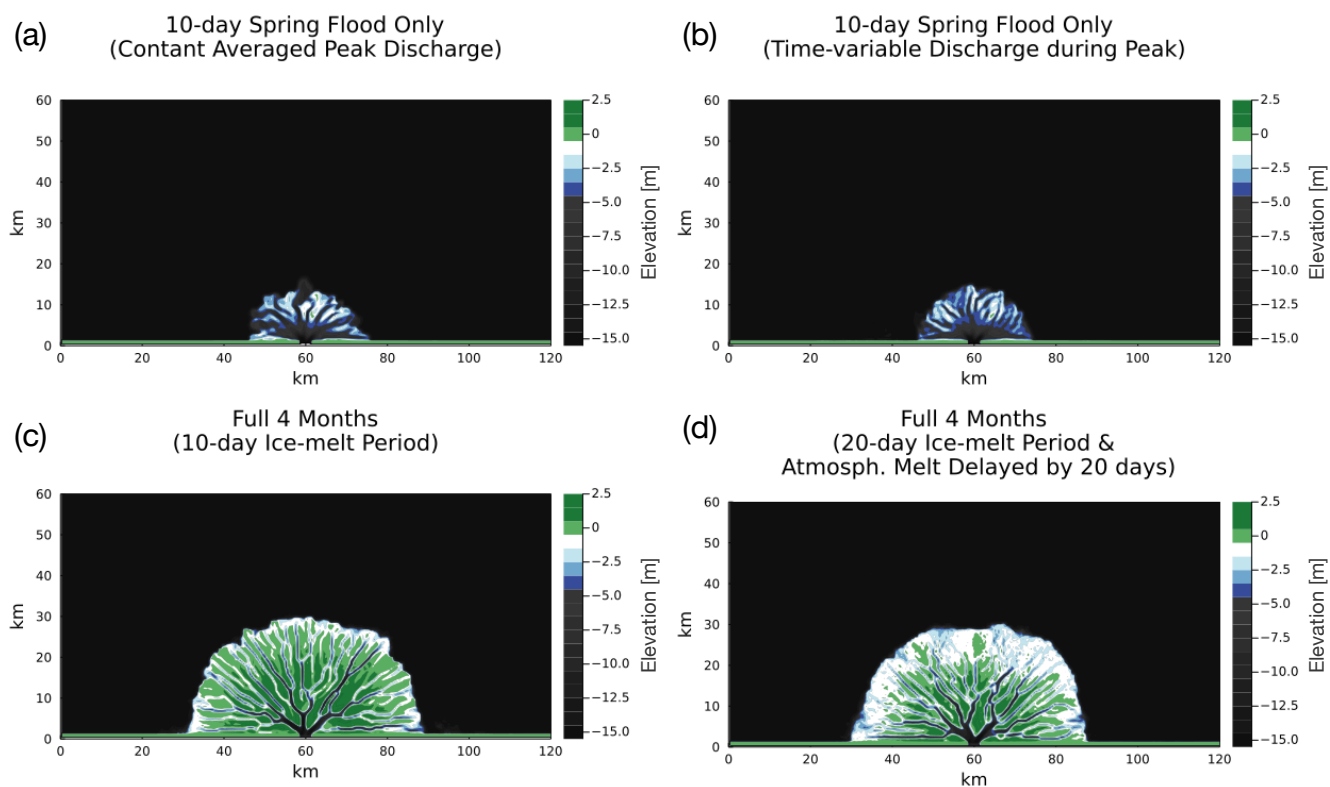
Figure 7. Bed elevations of deltas produced by running ArcDelRCM.jl for 150 model years on Lena-Delta-like spatial scales (see text in Sect. 3.3), with input discharge derived from daily measured values from GRDC Station Data 2903430 (2018). The top row (a, b) features deltas produced by running model years of 10 days each, which is also the ice-melt period. Discharge in these 10-day cases are taken from the peak 10 days of the time series and either (a) averaged and used as a constant value or (b) used directly as a 10-day discharge time series. The bottom row (c, d) features deltas that are produced by 4-month model years (June to September), using the full input discharge time series for the corresponding period. The case in panel c kept the ice-melt period of 10 days, whilst the case in panel d has an ice-melt period of 20 days and a delayed onset of atmospherically induced melting by 20 days from the start of each model year. Note the difference in size between the top and bottom rows, and the ramp feature around the delta in panel d.

Earth **Surface**
Dynamics
Discussions
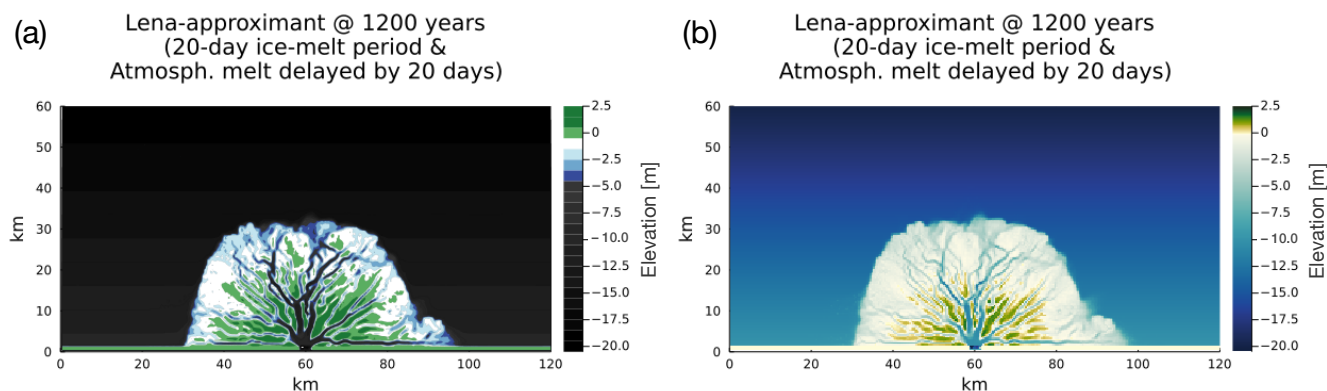
Figure 8. A delta produced by ArcDelRCM.jl after 1200 model years with configurations identical to those in Figure 7d, but with the low sediment-to-water volume ratio observed (Boike et al., 2019) and with a tilted ocean-basin bed motivated by the bathymetry of the Laptev Sea coast near the Lena Delta (see text in Sect. 3.3 for details). The panels show (a) the filled-contour view and (b) the gradient-coloured view of the same bed elevations.

Pathway (RCP) roughly 7 to 8.5 (Stocker, 2014), which corresponds to $\sim 4°C$ of global warming by the year 2100. Under this scenario, maximum ice thickness during winter is not expected to reduce drastically (Nummelin et al., 2016; Sun et al., 2018) although some thinning had been suggested (Landrum and Holland, 2020). We therefore adopt $h_{\text{ice,max}} = 1$ m thickness

360 instead of 2 m. The discharge at the Lena Delta has also been observed to be increasing in recent years (Fedorova et al., 2015). For this warming scenario, we also adopt an overall increase of 35 % in total discharge (Peterson et al., 2002), whilst the peaks remain the same (motivated by Juhls et al., 2020, in which they found an increased winter discharge; see also Mann et al., 2022). The overall time period during which discharge is over $20000 \text{ m}^3 \text{ s}^{-1}$ is 14 days longer. This modified discharge pattern is shown in Figure 6. Furthermore, based on the surface-temperature increase (and the rate of temperature increase

365 during the spring and summer months; Sun et al., 2018), the atmospheric heat-induced melting of ice cover is brought forward by 10 days and shortened in duration also by 10 days. All other parameters remain the same as described in Sect. 3.3.

  Figure 9 shows various snapshots of the continued evolution of the Lena-approximant delta. Under the warm conditions, the ramp feature has diminished by the 200-year mark (Figure 9a), and becomes mostly disrupted by the 400-year mark (Figure 9b). From 800 years onwards, no continuous ramp feature remains (Figure 9c and 9d).

370 **4 Discussion**

The results (Figure 4) demonstrates that ArcDelRCM.jl is able to reproduce the 2-m ramp around Arctic deltas (contrast with Figure 4a), and Figure 4d shows that the ramp is related to the maximum ice thickness ($h_{\text{ice,max}}$). Whilst off-shore depositions do occur as tentacle-like features in DeltaRCM-Arctic when relatively thick ice is imposed on a shallow domain ($h_{\text{ice,max}}/h_B = 3/5$; Figure 4c) as observed in Piliouras et al. (2021), our modifications in ArcDelRCM.jl led to similar features

375 in addition to a continuous ramp not limited to around channel outlets (Figure 4d). Increasing maximum ice extent to 100%

Earth **Surface**
Dynamics
Discussions
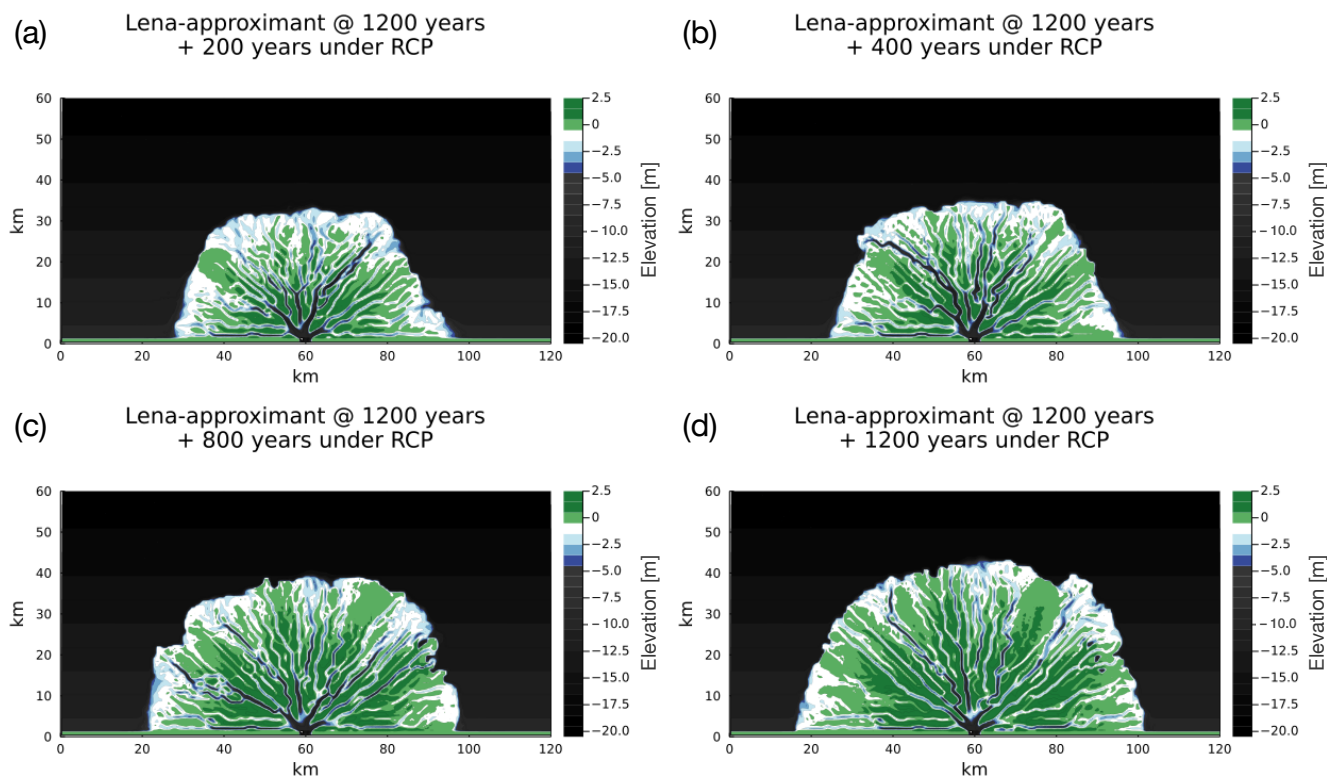
Figure 9. The continued evolution of the delta shown in Figure 8, except now under conditions possible in an end-member climate warming scenario (based roughly on RCP 7 to 8.5). As before, coloured contours reflect the bed elevations. The four panels show (a) 200, (b) 400, (c) 800, and (d) 1200 model years into this continued portion of the simulation. Note the degradation and disappearance of the ramp feature.

led to a more prominent ramp (Figure 4f), further supporting that ice is the driving factor behind the ramp feature. However, having a deeper ocean basin (i.e., more accommodation space) appears to impede the development of the ramp, as seen in Figure 4e (in stark contrast to Figure 4d). This suggests that the available space under maximum ice thickness ($h_{\text{ice,max}}$), and thus the dynamics of transport under ice cover around the shore of deltas plays a determining role in the formation of ramp

380 features. The less space there is, the more flow is constricted and the faster sediments build up against the bottom of the ice cover, forcing lateral deposition, which forms a continuous band that becomes the ramp feature.

Figure 5 shows the various effects of individual modifications detailed in section 2.2. Using the original DeltaRCM-Arctic model (Figure 5a) as baseline, limiting erosion to thawed layers whilst keeping a static thaw depth (Figures 5c and 5d) and foregoing the erodibility factor have the effect of allowing existing channels to erode more easily down to the thaw depth.

385 This reduces hindrances to the flow and leads to more sediments being carried farther seaward along the same channel paths, resulting in tentacle-like depositions. Further making the thaw depth time-dependent (as in Figures 5e and 5f), erosion can still occur (without the erodibility factor) down to the thaw depth, but the thaw depth now stays shallower throughout (approxi-

mately between 0.1 and 0.2 m). This leads to similar characteristics with the cases in Figures 5c and 5d in the central (ice-free) part of the delta, but the shallower erodible depth combined with ice constrictions are more able to force water pathways to

390 shift laterally close to the shore. Sediments are now deposited in a more evenly spread pattern, although some tentacle-like features remain. This deposition pattern would be the building block of a ramp feature, but in these cases they get deposited over quickly as the delta grows seaward, rather than being preserved.

The cases where the thaw-depth erosional limit is included in the bed-diffusion process (Figures 5d and 5f) do not appear to be substantially different from the cases where it is excluded (Figures 5c and 5e). This is expected because bed-diffusion has a

395 relatively minor effect on the delta's form compared to the flow-driven erosion and deposition.

The ice-shielding case (Figure 5g) has identical erosion mechanisms as in DeltaRCM-Arctic (Figure 5a), except erosion and deposition are blocked wherever ice is bedfast. This enhances flow constriction by ice, which focuses erosion on the few unblocked pathways, and leads to sediments being carried farther seaward. The result is a tentacle-like deposition pattern similar to Figures 5c and 5d, although the underlying mechanisms differ.

400 Figure 5h shows that the protection of bed-fast ice from flow-induced melting (Sect. 2.2.1) is ultimately the modification that gave the model the ability to produce the ramp feature. In this case, the erosion/deposition regime is the same as in the ice-shielding case (Figure 5g), giving a similar but less pronounced tentacle pattern. However, the bedfast ice, which is widespread on ramp features due to its depth being determined by ice thickness, survives for longer. This gives rise to two effects: (i) blocking or constriction by ice forces small lateral shifts in water pathways resulting in more even spreading of

405 depositions along the shore (similar to the cases of Figures 5e and 5f); (ii) the longer-lived bedfast ice protects the previously deposited material, allowing depositional lobes to expand and merge subaqueously without filling in to prograde the subaerial delta shoreline. The ramp feature is formed as a result.

Many of the individual modifications are made to ensure logical consistency. For instance, the protection of the bed by bed-fast ice (Sect. 2.2.1) and limiting erosion to only thawed layers (Sect. 2.2.3) directly follow from the protection of bed-fast ice

410 from flow-induced melting. Time-dependent thaw depth (Sect. 2.2.2) also becomes necessary due to the fact that bed-fast ice transfers heat conductively during winter months and delays the progression of the thaw depth during a model year, reducing erosion even during summer months. The combined effects of the individual modifications described above are what give rise to the form of the simulated deltas with ramp features in ArcDelRCM.jl (Figure 5b).

Interestingly, the graph metrics calculated from ensemble runs of 105 simulations for each of the cases described in Figure

415 5 are statistically indistinguishable from each other (Figure C1). This remains true even when we include the non-Arctic DeltaRCM in the analysis. This suggests that the stochastic nature of the model leads to more intrinsic variability than any potential systematic biases between cases with different modifications made to them. The fact that DeltaRCM and DeltaRCM-Arctic show statistically indistinguishable metrics suggests that the Arctic conditions considered do not have a noticeable effect on the overall structure of the channel network. Future work could apply more complex graph analyses to discern any subtler

420 differences in network structure or examine the topographic differences between these different Arctic delta models.

Figure 7 demonstrates the importance of delta activities outside of the peak flooding season. The discharge of large drainage basins such as the Lena watershed remains significant during the summer months (about 53% of the annual discharge; Holmes

et al., 2012), even though it is at a much lower level compared to the peak (GRDC Station Data 2903430, 2018, and Figure 6). The deltas produced by taking into account the summer months are 4 times the area (and more if one considers only above-

425 water areas) of the equivalent ones that take into account only the peak flooding period. Whether a constant discharge or a time-variable one is used during the peak period does not appear to have an impact on overall areal extent (Figures 7a and 7b).

Regarding the ramp feature, not only is it affected by the under-ice depth of the ocean basin, but also by the timing of the ice-melt. This is demonstrated in Figures 7c and 7d. By adopting a delayed onset of atmospherically induced melting, the ramp feature begins to emerge. This corresponds to how bed-fast ice resting on the ramp feature remains in place whilst the

430 ice in other areas of the delta is flushed or melted away, and only starts to break up after the peak flood is over (Figure 3). However, the deeper ocean and the different discharge pattern led to slower build-up of deposits during ice cover and more depositions during ice-free summer, resulting in the ramp being more hummocky and unevenly graded than in the small-scale, "benchmark" cases in Sect. 3.1.

In reality, the Lena Delta has a much lower sediment volume discharge (roughly a tenth) than we used in our demonstration

435 cases in Figure 7. The ocean bed on which it formed may not have been flat, but rather tilted from the coast towards the Laptev Sea. Taking these into account, the simulation in Figure 8 took 8 times as long to produce a delta with a size similar to the one in Figure 7d, but with a more pronounced ramp feature. This is consistent with the aforementioned observation that available depth below ice plays an important role in the formation of ramp features.

We note, however, that important ocean-driven processes are missing in the model, resulting in differences in smoothness

440 and outer-edge shapes between the modelled ramps and those observed in reality (Figure 1). Waves and tides likely play an important role in sculpting the ramp features. Moreover, compared to the deltas produced by DeltaRCM-Arctic and ArcDel-RCM.jl, the observed slopes of the sediment bed beyond the outer-edge of the 2-m ramps are much gentler, typically dipping from 2 m to > 20 m over $\mathcal{O}(10)$ km rather than $\mathcal{O}(0.1)$ km (Reimnitz, 2002; Are et al., 2002). This may have resulted from the limitation of having abrupt thresholds for deposition (Sect. 2.1.4) and in the classification of "on-delta" and "ocean" grid

445 cells during the flow routing (Sect. 2.1.2), in which most of the sediments carried in a packet tend to get deposited as soon as it leaves the "on-delta" cells. Future work on the model could focus on improving the capability of offshore dynamics, such that a full picture of a delta's formation and destruction can be built.

Finally, Figures 8 and 9 suggest that, under an estimated discharge and ice-cover pattern based on a strong warming scenario, an existing ramp feature could degrade on a time scale of centuries (Figures 9a and 9b), and effectively disappear within a

450 millennium (Figures 9c and 9d). Ocean processes may accelerate these time scales. The degradation of the subaqueous ramp could affect transport distance of sediments, impacting the release or sequestration of soil organic carbon (Overeem et al., 2022). The reduction of the shallow-water platform provided by the ramp can also impact the delta ecosystems (Lopez et al., 2006). Deltas will also lose a potentially important buffer against coastal erosion (Dean and Dalrymple, 2002).

5   Conclusions

455   We have written the ArcDelRCM.jl model in the Julia programming language and made the source code publicly available. ArcDelRCM.jl is based on the published descriptions of DeltaRCM-Arctic (Lauzon et al., 2019; Piliouras et al., 2021) and DeltaRCM (Liang et al., 2015b), supplemented with close examinations of the source codes of the (non-Arctic) DeltaRCM for any unpublished details (Liang, 2015; Perignon, 2018). Benchmarking runs with the non-Arctic DeltaRCM in MATLAB and Python shows that the Julia-based ArcDelRCM.jl is approximately 2-6 times faster.

460   In terms of the physical-process modelling, ArcDelRCM.jl contains the following modifications over the base DeltaRCM-Arctic: (i) the protection of bed-fast ice from flow-induced melting; (ii) the shielding of the bed by bed-fast ice; (iii) time-dependent thaw depth; (iv) the limiting of all forms of erosion to thawed layers only (instead of using an erodibility factor); (v) the ability for users to specify the time-step size (with internal checks for numerical stability); (vi) the ability to use a time series for input discharge and its related parameters.

465   The first of these modifications directly led to the ability of the model to reproduce the 2-m ramp features observed in Arctic deltas (Reimnitz, 2002). The second through fourth modifications in the list are developed for logical consistency with the first, and contribute individually to the under-ice deposition pattern and its subsequent preservation required for the ramp feature to form.

We have found that the ramp feature is indeed related to the winter ice cover, with its depth determined by the maximum
470   thickness of winter ice. We have also found that the prominence of this ramp feature is affected by three factors: (i) the thickness and extent of winter ice, (ii) the available depth in the ocean basin under the winter ice (i.e., accommodation space), and (iii) the timing of the melting of bed-fast ice from atmospheric heat. Specifically, the less under-ice depth is available for the delta to grow, the more prominent the ramp feature. Simulations of Lena-scale deltas also suggest that a delayed onset of atmospheric melting of bed-fast ice, which is widespread on the ramp feature, plays an important role in the formation and growth of the
475   ramp feature. The bed-fast ice protects the ramp from degradation during peak flow.

We found through graph analysis that the structures of channels, in terms of basic graph metrics, are statistically indistinguishable between the DeltaRCM-Arctic model, all individual modifications leading up to ArcDelRCM.jl, and ArcDelRCM.jl itself. This is true even when we included the non-Arctic DeltaRCM, indicating that the Arctic processes considered are not influencing the network structure of delta channels significantly.

480   Through the ability to specify time-step size directly and the use of time series for discharge inputs, we have demonstrated that the periods outside of the peak spring-flood season are significant contributors to an Arctic delta's evolution and thus cannot be neglected. In a set of Lena-like simulations, we found that the inclusion of summer months (from June to September), instead of limiting to the peak-flood period of 10 days, led to a quadrupling of the delta area under similar conditions.

When compared to bathymetry data, the simulation-produced ramp features have different elevation smoothness and outer-
485   edge shapes (i.e., the underwater "shorelines"). This may be due to the lack of ocean processes in the model and to the clear distinctions between "delta" and "ocean" grid cells. Future work could focus on addressing this limitation in order to improve the model's capability in predicting the future of Arctic deltas under an increasingly warm climate.

Earth **Surface**
Dynamics
Discussions
EGU
In a sequential pair of simulations (lasting millennia in model time) meant to closely mimic the Lena Delta under present-day and future ice and discharge conditions, we found that a formed ramp feature can degrade and effectively disappear on
490 a time scale of centuries under an extreme climate-warming scenario. This time scale could be accelerated further by ocean processes not included in the current model. Such degradation and disappearance of the ramp feature can impact the transport of carbon-carrying sediments, affect the delta ecosystems, and reduce future buffering of Arctic delta shorelines against coastal erosion.

Code availability. The source code of ArcDelRCM.jl is available via https://gitlab.com/nhchan/arcdelrcm.jl, and the source codes used for
495 the graph analyses are available via https://github.com/trettelbach/arctic_delta_analysis.

Appendix A: Other Feature Additions in ArcDelRCM.jl

A1 Inheritance of Simulation States

A convenience-motivated feature addition is the ability to start a simulation from an output state given by another simulation. This would allow users to investigate multiple change scenarios that occur after the formation of a delta, such as sudden
500 increase in discharge or in the duration of spring floods. This has been utilised in the case of Sect. 3.4. It could also be used to break very long simulations into stages to mitigate the risk of a computing-system crash.

A2 Pre-exisiting Island Blocks

Users can specify islands in the ocean basin of the simulation domain, where no physical processes can occur (similar to the inlet wall). This provides the ability to mimic, albeit simplistically, islands such as Arga in the Lena Delta. Geometries such as
505 rectangular and elliptical are available initially; more can be added in the future.

A3 Bed Geometries

The initial bed of the ocean basin can have non-uniform depths (i.e., variable h_B). Simple tilt geometries such as linear (from inlet side wall towards the ocean) and radial (from the centre of the inlet channel outwards) are available, in which users can specify the distance over which the ocean bed varies from a specified depth to the h_B specified in the simulation-domain
510 parameters. This has been utilised in Sect. 3.3 and 3.4.

Appendix B: The choice of initial positive degree day index

The simplistic initial value of $I = 10$ days is chosen by balancing a few factors that can vary over time and specific sites: (i) comparison between the daily temperatures at the Lena Delta extracted from the ERA-Interim reanalysis data (Dee et al., 2011) (Figure B1) and the approximate timing of a typical onset of the spring flood season there (around 1st June); (ii) the measured

515   water temperature in the Lena River showing that it crosses above $0°\mathrm{C}$ near the onset of the spring flood (Juhls et al., 2020); and (iii) the fact that all the simulated cases start when discharge is above a certain threshold (either covering the peak 10 days or when the discharge rises above $20000\ \mathrm{m^3s^{-1}}$; details in Section 3), which occur some days after the temperature becomes positive.
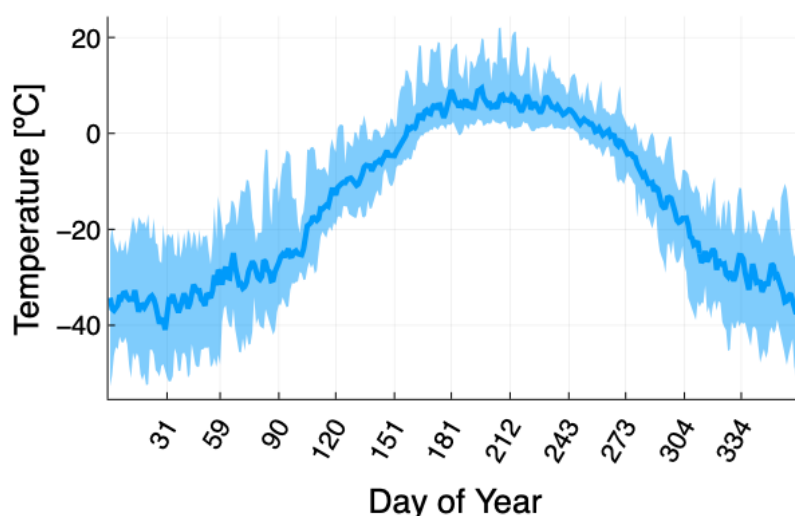
Figure B1. Daily temperature extracted from ERA-Interim reanalysis data (Dee et al., 2011) and averaged over all years from 1951 to 1980 (i.e., the same period from which the average daily discharge in Figure 6 is obtained). The lighter-shaded ribbon around the average line shows the range of daily temperatures during the same period.

Appendix C: Graph Analysis

520   We applied the algorithm of Rettelbach et al. (2021) to represent the deltas' channel topologies as graphs on an ensemble of 105 simulations of each of the eight cases shown in Figure 5, plus the non-Arctic DeltaRCM (not shown). Six basic metrics are shown here: the number of nodes and the number of edges of the graphs, the number of subgraphs (e.g., from abandoned channel networks), the graph density (i.e., the ratio of actual connections over the number of all possible connections), maximum diameter reached by the delta, and the length of all channels combined. The variability within each case far outweighs any possible differences between cases.

Appendix D: Data-structure Implementation of Sediment Records in ArcDelRCM.jl

Instead of a three-dimensional grid, we designed a data structure to record deposited sediments such that it is both memory-efficient and allows for fast access of individual sediment cells in a computer's memory (Figure D1).

Earth **Surface**
Dynamics
Discussions
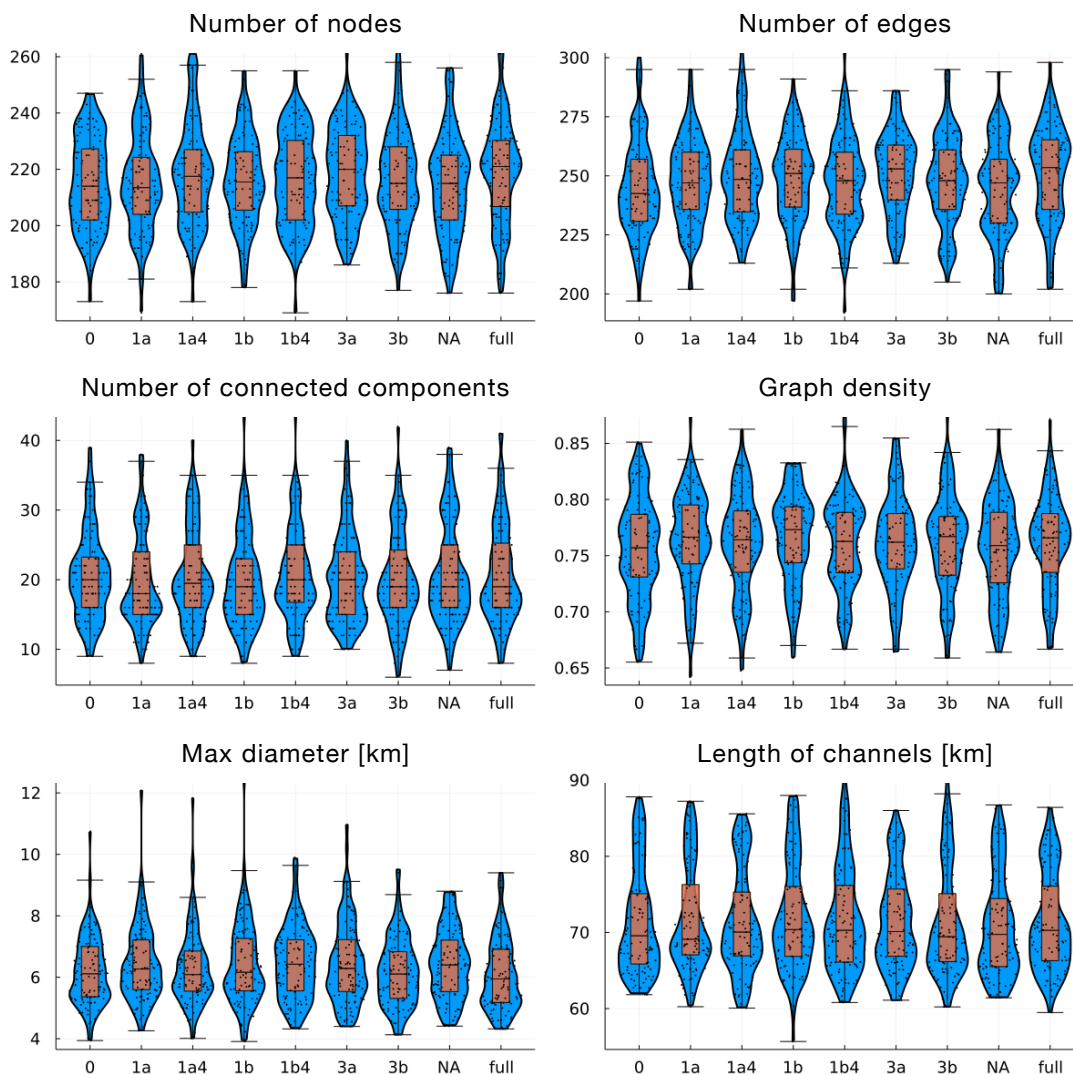
Figure C1. Plots showing delta metrics determined by the graph analysis we performed on each of the configurations described in Section 3.2. The blue violin plots show the kernel density estimate, the orange box and whisker plots show the central 50%, maximum, median, and minimum values, and the black dots show the actual values of the individual simulations. The labels are as follows: "0" denotes DeltaRCM-Arctic without modifications; "1a" denotes the case with erosion limited to thawed layers over a static thaw depth (Figure 5c); "1a4" denotes the same case as "1a", except the thaw depth is time-dependent (Figure 5e); "1b" and "1b4" correspond with "1a" and "1a4", respectively, except the effects are included in the bed-diffusion process (Figures 5d and 5f); "3a" denotes the case with ice-shielding of the bed (Figure 5g); "3b" denotes the case with both ice-shielding of the bed and the protection of bed-fast ice (Figure 5h); "NA" denotes the non-Arctic DeltaRCM case; and "full" denotes the full ArcDelRCM.jl case (Figure 5b).
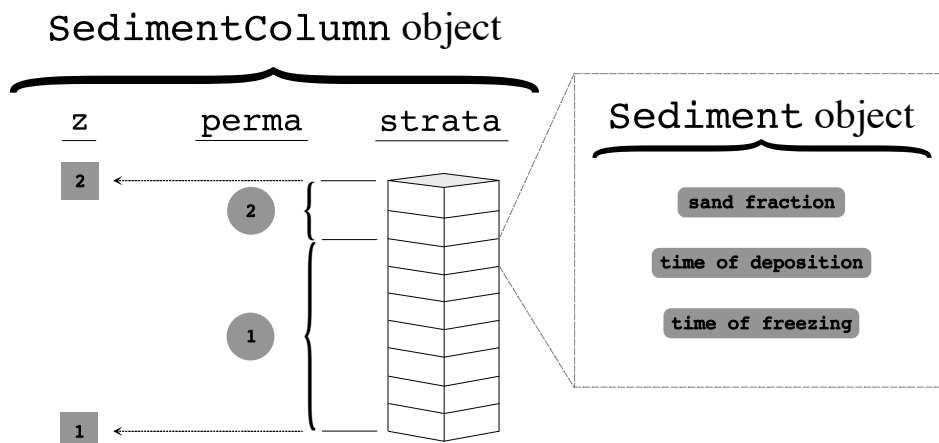
Figure D1. The storage scheme we designed for deposited sediments in ArcDelRCM.jl. In addition to sand fraction, we additionally store the time of deposition and time of freezing (if applicable) simultaneously. Each pixel in the simulation domain contains a `SedimentColumn` type object, which contains three vectors: `z`, with elements 1 and 2 being the bottom and top elevations of the column, respectively (grey numbered squares); `perma`, with element 1 being the thickness of the frozen layer and element 2 being the thickness of the thawed layer (grey numbered circles); and a vector of variable length, `strata`, in which each element is a `Sediment` type object. In each `Sediment` type object, three values are stored: sand fraction, time of deposition, and (if applicable) time of freezing of that specific element. The data structure is designed to reduce the empty cells that need to be stored in memory whilst keeping individual elements efficient to access.

Author contributions. The initial idea came from Langer, Braun, and Huppert. Chan wrote the source codes for all the delta models in Julia, led the scientific modifications that led to ArcDelRCM.jl, obtained the GRDC discharge data, and executed all the model simulations. He also drafted the initial text of the article and made all the figures except 1 and 3. Huppert and Braun provided the background and guidance for Chan during the early phase. Langer participated throughout the project and provided guidance and domain knowledge on permafrost and the Arctic, provided the ERA temperature data, and put Chan in communication with Juhls, Rettelbach, and Overduin. Overduin and Juhls gave expert knowledge of Arctic deltas and brought the ramp features to the other co-authors' attention. Juhls provided data and references regarding bathymetry, ice breakup, and water temperature. Juhls also made Figures 1 and 3. Rettelbach provided the codes and expertise related to the graph analyses. All authors contributed to subsequent editing of the draft manuscript.

Acknowledgements. Moritz Langer is supported through a grant by the Federal Ministry of Education and Research (BMBF) of Germany (No. 01LN1709A, Research Group PermaRisk). Chan thanks Laurens Bouwer from the Climate Service Center Germany (GERICS), part of

540   the Helmholtz-Zentrum Geesthacht, for pointing him to the GRDC discharge data during a chat in a workshop event. We also acknowledge the use of imagery from the NASA Worldview application (https://worldview.earthdata.nasa.gov/), part of the NASA Earth Observing System Data and Information System (EOSDIS).

References

Are, F., Grigoriev, M. N., Hubberten, H.-W., Rachold, V., Razumov, S. O., and Schneider, W.: Comparative Shoreface Evolution along the Laptev Sea Coast, Polarforschung, 70, 135–150, https://doi.org/10.1594/PANGAEA.425282, 2002.

Boike, J., Nitzbon, J., Anders, K., Grigoriev, M., Bolshiyanov, D., Langer, M., Lange, S., Bornemann, N., Morgenstern, A., Schreiber, P., Wille, C., Chadburn, S., Gouttevin, I., Burke, E., and Kutzbach, L.: A 16-Year Record (2002–2017) of Permafrost, Active-Layer, and Meteorological Conditions at the Samoylov Island Arctic Permafrost Research Site, Lena River Delta, Northern Siberia: An Opportunity to Validate Remote-Sensing Data and Land Surface, Snow, and Permafrost Models, Earth System Science Data, 11, 261–299, https://doi.org/10.5194/essd-11-261-2019, 2019.

Dean, R. G. and Dalrymple, R. A.: Coastal Processes: With Engineering Applications, Cambridge University Press, Cambridge, UK : New York, 2002.

Dee, D. P., Uppala, S. M., Simmons, A. J., Berrisford, P., Poli, P., Kobayashi, S., Andrae, U., Balmaseda, M. A., Balsamo, G., Bauer, P., Bechtold, P., Beljaars, A. C. M., van de Berg, L., Bidlot, J., Bormann, N., Delsol, C., Dragani, R., Fuentes, M., Geer, A. J., Haimberger, L., Healy, S. B., Hersbach, H., Hólm, E. V., Isaksen, L., Kållberg, P., Köhler, M., Matricardi, M., McNally, A. P., Monge-Sanz, B. M., Morcrette, J.-J., Park, B.-K., Peubey, C., de Rosnay, P., Tavolato, C., Thépaut, J.-N., and Vitart, F.: The ERA-Interim Reanalysis: Configuration and Performance of the Data Assimilation System, Quarterly Journal of the Royal Meteorological Society, 137, 553–597, https://doi.org/10.1002/qj.828, 2011.

Fedorova, I., Chetverova, A., Bolshiyanov, D., Makarov, A., Boike, J., Heim, B., Morgenstern, A., Overduin, P. P., Wegner, C., Kashina, V., Eulenburg, A., Dobrotina, E., and Sidorina, I.: Lena Delta Hydrology and Geochemistry: Long-Term Hydrological Data and Recent Field Observations, Biogeosciences, 12, 345–363, https://doi.org/10.5194/bg-12-345-2015, 2015.

Fuchs, M., Palmtag, J., Juhls, B., Overduin, P. P., Grosse, G., Abdelwahab, A., Bedington, M., Sanders, T., Ogneva, O., Fedorova, I. V., Zimov, N. S., Mann, P. J., and Strauss, J.: High-Resolution Bathymetry Models for the Lena Delta and Kolyma Gulf Coastal Zones, Earth System Science Data, accepted, https://doi.org/10.5194/essd-2021-256, 2021.

Gauckler, P.: Etudes Théoriques et Pratiques sur l'Ecoulement et le Mouvement des Eaux, Comptes Rendues de l'Académie des Sciences, 64, 818–822, 1867.

GRDC Station Data 2903430: STOLB Station Daily Data from 1951-2002, The Global Runoff Data Centre, 56068 Koblenz, Germany, 2018.

Holmes, R. M., McClelland, J. W., Peterson, B. J., Tank, S. E., Bulygina, E., Eglinton, T. I., Gordeev, V. V., Gurtovaya, T. Y., Raymond, P. A., Repeta, D. J., Staples, R., Striegl, R. G., Zhulidov, A. V., and Zimov, S. A.: Seasonal and Annual Fluxes of Nutrients and Organic Matter from Large Rivers to the Arctic Ocean and Surrounding Seas, Estuaries and Coasts, 35, 369–382, https://doi.org/10.1007/s12237-011-9386-6, 2012.

Hugelius, G., Strauss, J., Zubrzycki, S., Harden, J. W., Schuur, E. A. G., Ping, C. L., Schirrmeister, L., Grosse, G., Michaelson, G. J., Koven, C. D., O'Donnell, J. A., Elberling, B., Mishra, U., Camill, P., Yu, Z., Palmtag, J., and Kuhry, P.: Estimated Stocks of Circumpolar Permafrost Carbon with Quantified Uncertainty Ranges and Identified Data Gaps, Biogeosciences, 11, 6573–6593, https://doi.org/10.5194/bg-11-6573-2014, 2014.

Juhls, B., Stedmon, C. A., Morgenstern, A., Meyer, H., Hölemann, J., Heim, B., Povazhnyi, V., and Overduin, P. P.: Identifying Drivers of Seasonality in Lena River Biogeochemistry and Dissolved Organic Matter Fluxes, Frontiers in Environmental Science, 8, 53, https://doi.org/10.3389/fenvs.2020.00053, 2020.

Juhls, B., Antonova, S., Angelopoulos, M., Bobrov, N., Grigoriev, M., Langer, M., Maksimov, G., Miesner, F., and Overduin, P. P.: Serpentine (Floating) Ice Channels and Their Interaction with Riverbed Permafrost in the Lena River Delta, Russia, Frontiers in Earth Science, 9, 689 941, https://doi.org/10.3389/feart.2021.689941, 2021.

Landrum, L. and Holland, M. M.: Extremes Become Routine in an Emerging New Arctic, Nature Climate Change, 10, 1108–1115, https://doi.org/10.1038/s41558-020-0892-z, 2020.

Lauzon, R., Piliouras, A., and Rowland, J. C.: Ice and Permafrost Effects on Delta Morphology and Channel Dynamics, Geophysical Research Letters, 46, 6574–6582, https://doi.org/10.1029/2019GL082792, 2019.

Lesser, G. R., Roelvink, J. A., van Kester, J. A. T. M., and Stelling, G. S.: Development and Validation of a Three-Dimensional Morphological Model, Coastal Engineering, 51, 883–915, https://doi.org/10.1016/j.coastaleng.2004.07.014, 2004.

Liang, M.: DeltaRCM [Source Code in CSDMS GitHub Repository], https://github.com/csdms-contrib/DeltaRCM, 2015.

Liang, M., Geleynse, N., Edmonds, D. A., and Passalacqua, P.: A Reduced-Complexity Model for River Delta Formation — Part 2: Assessment of the Flow Routing Scheme, Earth Surface Dynamics, 3, 87–104, https://doi.org/10.5194/esurf-3-87-2015, 2015a.

Liang, M., Voller, V. R., and Paola, C.: A Reduced-Complexity Model for River Delta Formation — Part 1: Modeling Deltas with Channel Dynamics, Earth Surface Dynamics, 3, 67–86, https://doi.org/10.5194/esurf-3-67-2015, 2015b.

Lopez, C. B., Cloern, J. E., Schraga, T. S., Little, A. J., Lucas, L. V., Thompson, J. K., and Burau, J. R.: Ecological Values of Shallow-Water Habitats: Implications for the Restoration of Disturbed Ecosystems, Ecosystems, 9, 422–440, https://doi.org/10.1007/s10021-005-0113-7, 2006.

Lunardini, V. J.: Heat Transfer in Cold Climates, Van Nostrand Reinhold Company, New York, 1981.

Mann, P. J., Strauss, J., Palmtag, J., Dowdy, K., Ogneva, O., Fuchs, M., Bedington, M., Torres, R., Polimene, L., Overduin, P., Mollenhauer, G., Grosse, G., Rachold, V., Sobczak, W. V., Spencer, R. G. M., and Juhls, B.: Degrading Permafrost River Catchments and Their Impact on Arctic Ocean Nearshore Processes, Ambio, 51, 439–455, https://doi.org/10.1007/s13280-021-01666-z, 2022.

Manning, R., Griffith, J. P., Pigot, T., and Vernon-Harcourt, L. F.: On the Flow of Water in Open Channels and Pipes, Transactions of the Institution of Civil Engineers of Ireland, 20, 161–207, 1890.

Nummelin, A., Ilicak, M., Li, C., and Smedsrud, L. H.: Consequences of Future Increased Arctic Runoff on Arctic Ocean Stratification, Circulation, and Sea Ice Cover, Journal of Geophysical Research: Oceans, 121, 617–637, https://doi.org/10.1002/2015JC011156, 2016.

Overeem, I., Nienhuis, J. H., and Piliouras, A.: Ice-Dominated Arctic Deltas, Nature Reviews Earth & Environment, 3, 225–240, https://doi.org/10.1038/s43017-022-00268-x, 2022.

Perignon, M.: pyDeltaRCM [Source Code in GitHub Repository], https://github.com/mperignon/pyDeltaRCM_WMT, 2018.

Peterson, B. J., Holmes, R. M., McClelland, J. W., Vörösmarty, C. J., Lammers, R. B., Shiklomanov, A. I., Shiklomanov, I. A., and Rahmstorf, S.: Increasing River Discharge to the Arctic Ocean, Science, 298, 2171–2173, https://doi.org/10.1126/science.1077445, 2002.

Piliouras, A., Lauzon, R., and Rowland, J. C.: Unraveling the Combined Effects of Ice and Permafrost on Arctic Delta Morphodynamics, Journal of Geophysical Research: Earth Surface, 126, https://doi.org/10.1029/2020JF005706, 2021.

Pisaric, M. F. J., Thienpont, J. R., Kokelj, S. V., Nesbitt, H., Lantz, T. C., Solomon, S., and Smol, J. P.: Impacts of a Recent Storm Surge on an Arctic Delta Ecosystem Examined in the Context of the Last Millennium, Proceedings of the National Academy of Sciences of the United States of America, 108, 8960–8965, https://doi.org/10.1073/pnas.1018527108, 2011.

Reimnitz, E.: Interaction of River Discharge with Sea Ice in Proximity of Arctic Deltas: A Review, Polarforschung, 70, 123–134, https://doi.org/10.2312/polarforschung.70.123, 2002.

Rettelbach, T., Langer, M., Nitze, I., Jones, B., Helm, V., Freytag, J.-C., and Grosse, G.: A Quantitative Graph-Based Approach to Monitoring Ice-Wedge Trough Dynamics in Polygonal Permafrost Landscapes, Remote Sensing, 13, 3098, https://doi.org/10.3390/rs13163098, 2021.

Riseborough, D., Shiklomanov, N., Etzelmüller, B., Gruber, S., and Marchenko, S.: Recent advances in permafrost modelling, Permafrost and Periglacial Processes, 19, 137–156, https://doi.org/10.1002/ppp.615, 2008.

620   Schuur, E. A. G., McGuire, A. D., Schädel, C., Grosse, G., Harden, J. W., Hayes, D. J., Hugelius, G., Koven, C. D., Kuhry, P., Lawrence, D. M., Natali, S. M., Olefeldt, D., Romanovsky, V. E., Schaefer, K., Turetsky, M. R., Treat, C. C., and Vonk, J. E.: Climate Change and the Permafrost Carbon Feedback, Nature, 520, 171–179, https://doi.org/10.1038/nature14338, 2015.

Searcy, C., Dean, K., and Stringer, W.: A River-Coastal Sea Ice Interaction Model: Mackenzie River Delta, Journal of Geophysical Research: Oceans, 101, 8885–8894, https://doi.org/10.1029/96JC00120, 1996.

625   Stocker, T., ed.: Climate Change 2013: The Physical Science Basis: Working Group I Contribution to the Fifth Assessment Report of the Intergovernmental Panel on Climate Change, Cambridge University Press, New York, 2014.

Sun, L., Alexander, M., and Deser, C.: Evolution of the Global Coupled Climate Response to Arctic Sea Ice Loss during 1990–2090 and Its Contribution to Climate Change, Journal of Climate, 31, 7823–7843, https://doi.org/10.1175/JCLI-D-18-0134.1, 2018.